THESIS FOR THE DEGREE OF DOCTOR OF PHILOSOPHY

Influence of total pressure on complete oxidation of methane over Pd/Al_2O_3 catalysts

Experimental studies and multiscale simulations

CARL-ROBERT FLORÉN

CHALMERS

Department of Chemistry and Chemical Engineering
CHALMERS UNIVERSITY OF TECHNOLOGY
Gothenburg, Sweden 2019

Influence of total pressure on complete oxidation of methane over Pd/Al_2O_3 catalysts
Experimental studies and multiscale simulations
Carl-Robert Florén

ISBN 978-91-7905-225-6

Doktorsavhandlingar vid Chalmers tekniska högskola,
Ny serie nr. 4692
ISSN 0346-718X

Department of Chemistry and Chemical Engineering
Chalmers University of Technology
SE-412 96 Gothenburg
Sweden
Telephone +46 (0)31 772 1000

Cover:
Illustration of the multiscale model where the reactants, methane and oxygen, flow through an emission oxidation catalyst. The surface oxidation reaction is described by first-principles calculations and the product gases, water and carbon dioxide, exits the catalyst.

Typeset in LaTeX
Printed by Chalmers Reproservice
Gothenburg, Sweden 2019

Influence of total pressure on complete oxidation of methane over Pd/Al_2O_3 catalysts
Experimental studies and multiscale simulations

Carl-Robert Florén
Department of Chemistry and Chemical Engineering
Chalmers University of Technology

Abstract

Natural gas and biogas, which have methane as their main component, are interesting choices of fuel to reduce the anthropogenic emissions of greenhouse gases. However, as methane is a greenhouse gas, uncombusted methane should be removed from the combustion gases. Emission control catalysts can preferably be used to completely oxidise methane. This thesis aims to examine whether an increased total pressure can be utilized to enhance the methane oxidation reaction over Pd/Al_2O_3 catalysts. The effects of total pressure are studied by flow-reactor experiments and simulations. The prepared catalyst samples are characterised by N_2-physisorption, CO-chemisorption and diffusive reflectance infrared Fourier transform spectroscopy.

A multiscale model is developed to simulate the activity of methane oxidation over Pd/Al_2O_3 where the reaction kinetics are based on first-principles calculations. The results show that the oxidation of methane can be enhanced when the total pressure is increased above atmospheric pressure. However, the effect depends on the gas composition and reaction temperature. In a dry and oxygen rich feed gas composition, the activity benefits from an increased total pressure over the entire examined temperature range. The positive effect is attributed to a high fraction of available under-coordinated palladium and oxygen sites, which can dissociate the increased concentration of methane. When water or carbon dioxide is present in the feed gas these molecules adsorb on the under-coordinated palladium sites and through surface reactions block the palladium atom as adsorbed water, hydroxyl species and bicarbonate. The coverage of hindering species requires a higher temperature to regain available palladium and oxygen sites and the positive total pressure dependence on the oxidation of methane. If the temperature is too low, the simulations predict a negative effect of increased total pressure on the reaction. The multiscale simulations capture the experimental trends and indicate that support effects should be incorporated to the model for a more complete reaction mechanism.

Keywords: methane oxidation, total pressure, Pd/Al_2O_3, multiscale flow-reactor model

List of Publications

This thesis is based on the following appended papers:

I. Total oxidation of methane over Pd/Al_2O_3 at pressures from 1 to 10 atm
C-R. Florén, C. Demirci, P-A. Carlsson, D. Creaser and M. Skoglundh
In manuscript

II. Modelling complete methane oxidation over palladium oxide in a porous catalyst using first-principles surface kinetics
C-R. Florén, M. Van den Bossche, D. Creaser, H. Grönbeck, P-A. Carlsson, H. Korpi and M. Skoglundh
Catalysis Science & Technology, **8** (2017), 508-520

III. Multiscale reactor modelling of total pressure effects on complete methane oxidation over Pd/Al_2O_3
C-R. Florén, P-A. Carlsson, D. Creaser, H. Grönbeck and M. Skoglundh
Catalysis Science & Technology, **9** (2019), 3055-3065

IV. Palladium dispersion effects on wet methane oxidation kinetics
P. Velin, C-R. Florén, M. Skoglundh, A. Raj, D. Thompsett, G. Smedler and P-A. Carlsson
Manuscript submitted

My Contributions to the Publications

Paper I
For this paper, I designed and constructed the flow reactor used for the pressurised experiments. I prepared the Pd/Al_2O_3 sample, planned and performed the activity measurements, performed all characterisation measurements except the ICP analysis, interpreted the results and wrote the first draft of the manuscript together with my (shared) first author. I was responsible for writing the manuscript and I performed all calculations.

Paper II
For this paper, I wrote and modified scripts and compiled them into a 1D porous washcoat model used for the simulations. I performed all calculations and interpreted the results together with my co-authors. I was responsible for writing the first draft of the manuscript. I was responsible the writing process and submitting the manuscript.

Paper III
I wrote the script and extended the previous 1D porous washcoat model into a 2D multiscale flow-reactor model used in this paper. I performed all calculations and interpreted the results together with my co-authors. I was responsible for writing the first draft of the manuscript. I was responsible for the writing process and submitting the manuscript.

Paper IV
I participated in the planning and performing of the experiments and co-authored the manuscript. I performed all simulations and wrote the corresponding discussion in the manuscript.

CONTENTS

CHAPTER 1

INTRODUCTION

1.1 A brief history of catalysis

Catalytic processes are present all around us in nature, with and without our knowledge. Two examples crutial for life are the photosynthesis where vegetation use carbon dioxide, water and energy from light to synthesise biomass, and the digestion process in our bodies where enzymes provide us with energy that is converted from the carbohydrates in the food. The fermentation process is another example known since ancient times where yeast is used to produce wine and beer [1]. At this time the actual process taking place was not known. The fist reported observation of a catalytic process, as we know it today, was in 1794 by the Scottish chemist named Elizabeth Fulhame [2]. Through her work she was led to believe that many oxidation reactions only occur in the presence of water which takes part in the reaction and is regenerated at the end of the reaction. Further, Fulhame is probably the first person to propose a modern type of reaction mechanism for the reactions she was studying [3]. Her theory was contradictory to the phlogiston theory of the time and it took 42 years until the Swedish chemist Jöns Jacob Berzelius, in 1836, published a review of previous findings. Berzelius realised that there is a yet unknown force that drives the reactions and introduced, without recognizing Fulhame's work, the word "catalysis" by discussing the presence of a catalytic force [2, 4]. The word catalysis originates from the greek words *kata*, meaning down, and *lyein* which means loosen [5, 6]. Today, we define a catalyst as a substance which increases the rate of a chemical reaction towards equilibrium without being consumed [7]. Our understanding of catalysis has increased since Berzelius' review and it has enabled many applications that we rely on today. Two important inventions during the last century, thanks to catalysis, are the Haber-Bosch process and the Fisher-Tropsch synthesis from 1918 and 1926, respectively. The two processes enabled production of

ammonia from nitrogen and hydrogen and liquid hydrocarbons from carbon monoxide and hydrogen [8, 9]. The ammonia production provided us with a new, and much more effective, way of producing fertilizers for our food crops, and the Fisher-Tropsch synthesis liquid hydrocarbons enabled production of synthetic oils and fuel (e.g. petrol and diesel) from coal.

1.2 Methane utilization

The extreme usage of coal during the industrial revolution in the 18th century led to a radical increase of the anthropogenic emissions of harmful compounds to the atmosphere. By then, the coal was necessary to power the industries but has over time been substituted for other energy carriers. As for today, two fuel sources showing an increased global interest are natural gas and biogas, which both mainly consist of methane with a dry content of around 90 and 60 %, respectively [10–13]. Biogas has a higher content of carbon dioxide and sulfuric compounds, and their exact concentrations depend on the production process. However, the sulfuric impurities can be partly removed, along with carbon dioxide and moisture, from the biogas which is then upgraded into biomethane. Biomethane is comparable to natural gas in composition and thus can be used as a drop-in fuel and be transported by the same infrastructure [14]. The combustion of natural gas, or biomethane, produces less carbon dioxide per unit of delivered energy and can preferably be used in the energy and transportation sectors to substitute other fossil fuels based on crude oil and coal, therefore reducing their environmental foot-print [15, 16]. Moreover, combustion of natural gas, as compared to petrol and diesel, benefits from reduced emissions of carbon dioxide, nitrous oxides, sulfur oxides and soot particles [17]. The drawback of using natural gas in combustion processes is the possible slip of methane caused by incomplete combustion. Because methane has a high global warming potential it is essential to remove traces of methane after the combustion process [18, 19]. A common and proven technology for the removal of methane is the use of emission catalysts [16]. Depending on the application type and the operating conditions, the catalyst must be designed for its specific purpose to show a satisfying performance. In the case of natural gas powered internal combustion engines, the purpose of the catalyst is to minimise harmful emissions of methane by complete oxidation, where the methane is converted into carbon dioxide. The abatement is however still challenging as the decomposition reactions of methane on the catalyst surface are slow at the relatively low temperatures of vehicle exhaust gases. Many industrial catalytic process are operated under elevated pressures because of favourable reaction kinetics resulting in increased conversion and/or selectivity. Examples are the Fischer-Tropsch synthesis which shows an increased carbon monoxide conversion at high pressure and

increased selectivity towards the wanted longer hydrocarbon chains [20]. Other examples include ammonia production [8], catalytic cracking [21] and methanol synthesis [22] which all show an increased conversion of reactant at elevated pressures. Similarly, several studies show that high-temperature catalytic methane combustion for heat and power generation preferably can be operated at elevated pressures [23–29]. This makes it tempting to install a methane oxidation catalyst for aftertreatment purposes between the engine and turbo charger which could be possible in a large engine system and take advantage of the elevated pressure. If the idea is proven feasible, it could reduce the necessary size of the catalytic system by increasing its performance [30, 31].

However, the literature is scarce about low-temperature oxidation of methane at elevated pressures, which is of interest for vehicle applications. The literature is exclusively targeting atmospheric pressure with few exceptions [25, 30–33]. Furthermore, the research focus has traditionally been targeted on understanding of the active sites of the catalyst and how to formulate more active and durable catalytic materials [34–48]. The above arguments motivate further research on methane oxidation at low temperatures and elevated pressures, to find and develop catalytic materials with higher performance. As for today, methane abatement in vehicle applications is generally performed by palladium based catalysts thanks to favorable kinetic properties towards complete methane oxidation.

1.3 Scope

The main objective of this work is to investigate if the performance of an alumina supported palladium based catalyst for complete methane oxidation is enhanced by increasing the total pressure above atmospheric pressure. The aim is investigated by a combination of theoretical and experimental methods including multiscale simulations, catalyst preparation, characterisation and kinetic experiments in lab scale flow-reactors.

In **Paper I** the influence of total pressure on methane oxidation over Pd/Al_2O_3 is investigated for a dry feed gas composition. The studies in **Paper II** and **Paper III** take on the theoretical approach and simulate the methane conversion through a monolithic reactor with the addition of water and/or carbon dioxide to the feed gas. The effects of adding water and carbon dioxide are discussed, and how these compounds affect the influences of total pressure are discussed. **Paper IV** brings up the deactivation effect of wet feed gas composition and compares the results to simulations at atmospheric pressure to evaluate the applicability of the model. **Paper IV** discusses the possible effects of support interactions, which are not considered in the simulations.

CHAPTER 2

CATALYSIS FOR COMPLETE METHANE OXIDATION

2.1 Heterogeneous catalysis

Catalysis is divided into two sub-groups, homogeneous and heterogeneous catalysis. In a homogeneous system, the catalyst and the reactants are in the same phase (solid, fluid or gas) whereas in a heterogeneous system they are instead in different phases. Heterogeneous catalysis is widely used in industry at for example the previously mentioned Haber-Bosch and Fisher-Tropsch processes to produce, e.g., fuels, fine chemicals and fertilizers. Another application where heterogeneous catalysis has become increasingly more important since the mid-20th century, are emission control systems to remove unwanted components from the exhaust of mobile and stationary sources [49, 50]. An upcoming technology that has started competing in the vehicle market is the fuel cell technology, which shows several promising applications [51]. Fuel cells are used to produce an electrical current, to power the application of interest, by converting hydrogen and oxygen into water [52].

The activation energy of a chemical reaction is the minimum required potential energy of the reactants to undergo a chemical transformation. As mentioned in the introduction, the catalyst increases the rate of a chemical reaction without being consumed itself in the process. This is achieved by a decreased, so called, activation energy for the reaction. Further, the activation energy is dependent on the reaction and the prevailing reaction conditions. This means that some reactions have a high energy demand in terms of high temperatures and/or pressures to take place. The catalyst lowers the activation energy of a reaction by providing an alternative reaction mechanism, which is less energy demanding, compared to the corresponding reaction without a catalyst. This is illustrated in Figure 2.1. It is however important to state that a catalyst do not

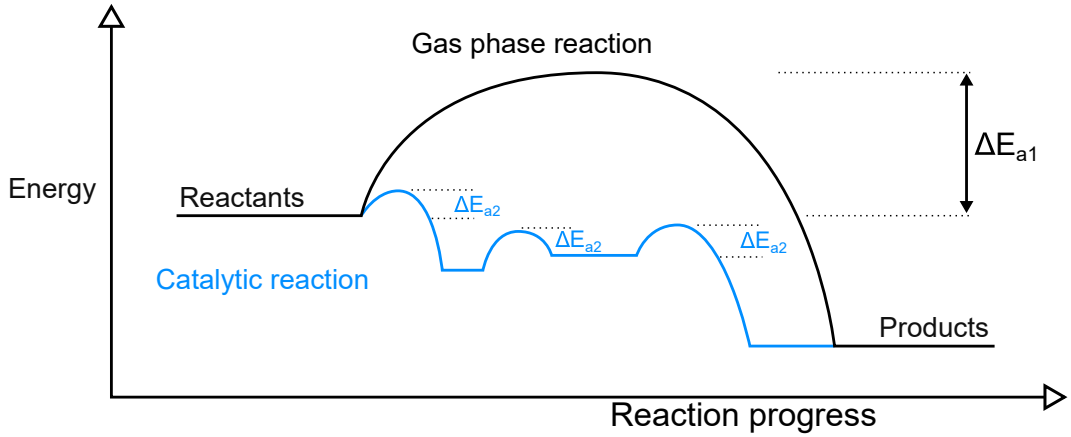

Figure 2.1: The catalyst lowers the activation energy of a gas phase reaction by providing an alternative and less energy demanding reaction pathway.

alter the thermodynamic properties of a chemical reaction, hence adding a catalyst does not effect a reaction that is thermodynamically inherently not feasible.

An example of heterogeneous catalytic reaction, in this case complete oxidation of methane with oxygen, and the different sub-processes are illustrated in Figure 2.2. First the reactants, methane and oxygen, must be transported from the bulk gas phase to the catalyst surface (external diffusion). From the catalyst surface the reactants are transported into the porous structure to the vicinity of an active site (internal diffusion). At the active site the methane and/or oxygen molecules, depending on the reaction mechanism, create chemical bonds to active site (adsorption) and through surface reaction form the products carbon dioxide and water (surface reaction). At this point, the products break their bonds to the active site (desorption) and diffuse through the porous structure to the surface boundary (internal diffusion) and ultimately from the surface into the bulk gas (external diffusion). The overall reaction process is only as fast as the slowest sub-process, which can be either one of the steps 1-7 in Figure 2.2. The slowest step in the reaction is referred to as the rate-limiting or rate determining step.

The material science of inorganic heterogeneous catalysis includes different parameters that can be tuned to optimise a chemical reaction. These parameters consider the active metal and its nanoparticle shape and size, alloys of different metals and the surrounding oxide support structure. Hence, a large number of catalyst designs have been developed over the years. Two examples of common oxide supports for emission catalysts, are zeolites and metal-oxide supports, onto which the active metal is deposited on surface. Both are solids and while the zeolites are acidic and benefit from a well-defined porous structure, the metal-oxide supports are simple to manufacture. Apart from the

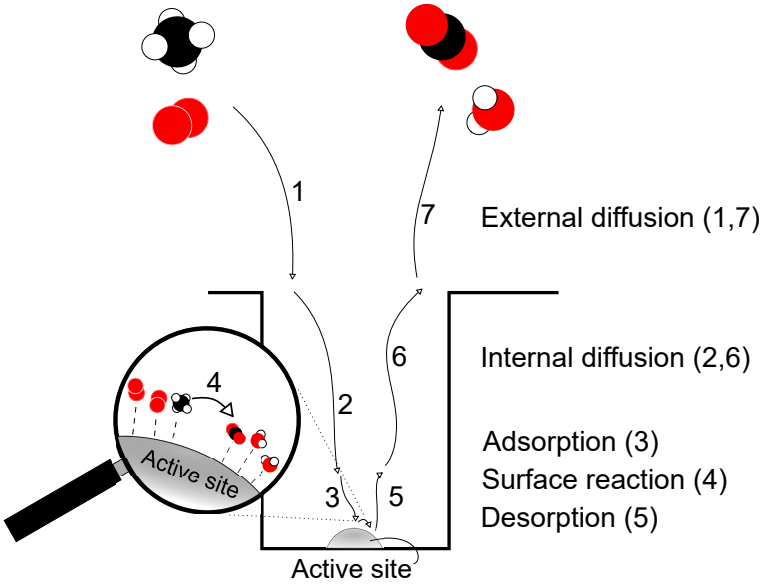

Figure 2.2: Illustration of the sub-processes of catalysed heterogeneous reaction over a solid particle in a porous support. The slowest step is called the rate-limiting or rate determining step.

catalyst design, the reactor vessel in which the catalyst is held, can be designed in various ways to optimise the reaction conditions around the catalytic material. This kind of optimisation is, especially if included on top of catalyst design, time consuming and included several parameters such as reactor vessel geometry, internal packing material, flow characteristics, type of catalyst and more. Reactor design will not be discussed further in this work and the interested reader is encouraged to read reference [53] to get an overview of reactor design.

2.2 The supported noble metal catalyst

This work is focusing on the supported noble metal catalyst because this type has been extensively used for emission control in vehicles and for methane oxidation applications where lower temperatures are of interest. Common metal-oxide support materials for methane oxidation include alumina (Al_2O_3), ceria (CeO_2), silica (SiO_2) and zirconia (ZrO_2) or combinations of these [42, 43, 54–57]. The metal-oxide supports are not alone catalytically active towards methane oxidation and require that the active metal is distributed onto their surfaces. This results in many different combinations and traditionally, platinum or palladium supported on metal-oxide supports have been used to catalyse the complete oxidation of methane. Platinum and palladium have been shown to efficiently catalyse and dissociate the symmetric and stable methane molecule [39, 42, 58–60]. Further, the alumina supported palladium catalyst (Pd/Al_2O_3) is reported to exhibit a high activity for complete methane oxidation at lower temperatures,

down to around 300 °C [39,42,61]. Despite showing a promising activity, Pd/Al_2O_3 has a low tolerance and stability to water and sulfur compounds [62–65]. These compounds affect the catalyst by blocking the active sites of the noble metal particles, making the active sites inaccessible for methane dissociation, and changing the structure of the support material by sintering. Both effects can lead to an irreversible loss of active sites and hence decreased activity. Sulfur compounds are present in trace amounts in the fuel and the content varies depending on the source and the production method. Water is commonly present in exhaust gases at roughly 5-10 vol.-% but is also a reaction product from the combustion of methane. Hence, water can inevitably be completely removed around the catalyst structure. During the last years an increased number of reports studying complete methane oxidation have focused on using zeolites instead of the metal-oxides as a support material thanks to their better hydrothermal stability [66–68]. These findings could hopefully lead to the development of new catalytic materials that can withstand long-term exposure of water vapour and trace compounds that are present in realistic exhaust gases from combustion engines.

2.3 Methane oxidation and activation

The overall chemical reaction formula for complete methane oxidation is shown in equation 2.1. The reaction is highly exothermic with a reaction enthalpy of -802 kJ/-mol which means that energy is released as methane is combusted. Without a catalyst present, the auto-ignition temperature for the complete methane oxidation is experimentally reported to be around 750 °C [69], as compared to the catalysed ignition temperature of ∼300 °C.

$$CH_4 + 2O_2 \rightleftharpoons CO_2 + 2H_2O \tag{2.1}$$

$$\Delta H_r = -802.3\ kJ/mol$$

Many studies for methane oxidation have been focused on understanding the nature and the different active sites present on the supported palladium metal particle. The palladium particle has several different surface facets which have different inherent reactivities towards methane dissociation [70–73]. It is still challenging to conclude which palladium surface is the most prominent under realistic reaction conditions and the reaction mechanism for a supported palladium based catalyst, under oxygen excess conditions, is still in debate. However, an oxidised state of the active palladium site (PdO) is expected in oxygen rich conditions and has been reported to possess high catalytic activity towards oxidizing methane [74–77]. Furthermore, the PdO(101) surface is reported as the most active surface facet of palladium oxide towards dissociative methane adsorption [76–79]. The PdO(101) surface is illustrated in Figure 2.3 using

a ball-and-stick model. The reaction mechanism for methane oxidation on the palladium oxide surface has been extensively discussed the last couple of decades [80]. It is today widely accepted that a Pd-O dimer is responsible for the dissociative adsorption of methane where a CH_3 and a surface hydroxyl species are formed [80–82]. The succeeding decomposition of CH_3, and ultimately formation of CO_2, proceeds by step-wise breaking of the C-H bonds and interaction with bulk gas oxygen and the metal-oxide support to regenerate the formed oxygen vacancies [77, 82–84].

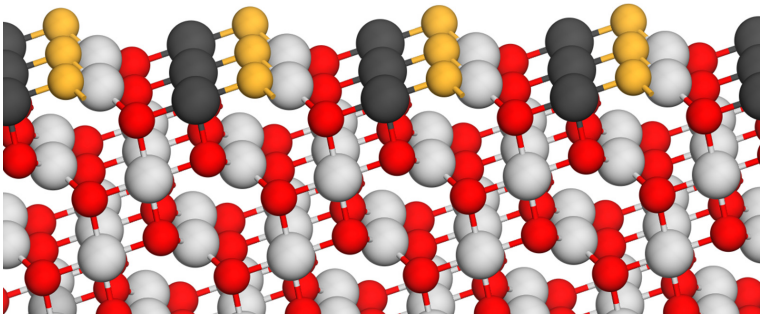

Figure 2.3: A ball-and-stick model of the PdO(101) surface. Here black is an under-coordinated Pd, yellow is an under-coordinated O while gray and red are the fourfold coordinated arrangements of Pd and O, respectively.

CHAPTER 3

RESEARCH APPROACH AND METHODS

3.1 Multiscale modelling

Catalytic reactions at industrial applications are dependent on achieving and maintaining the correct reaction conditions. Therefore it is important to understand the reaction process and its dependencies on external influences. To extend the knowledge about the reaction of catalytic system, the reaction network and kinetics can be described at the atomic scale by quantum mechanical calculations. Similarly, the molecular dynamics of the mass and heat transport can be described at the macro-scale by proper continuum equations of fluid motion. Figure 3.1 illustrates the different scales in time and length for a flow system. Such a model would consist of multiple 'sub-processes', each describing a process at a different scale and complexity, to describe the complete system from a broader perspective. The challenge lies in that the sub-processes must be coupled

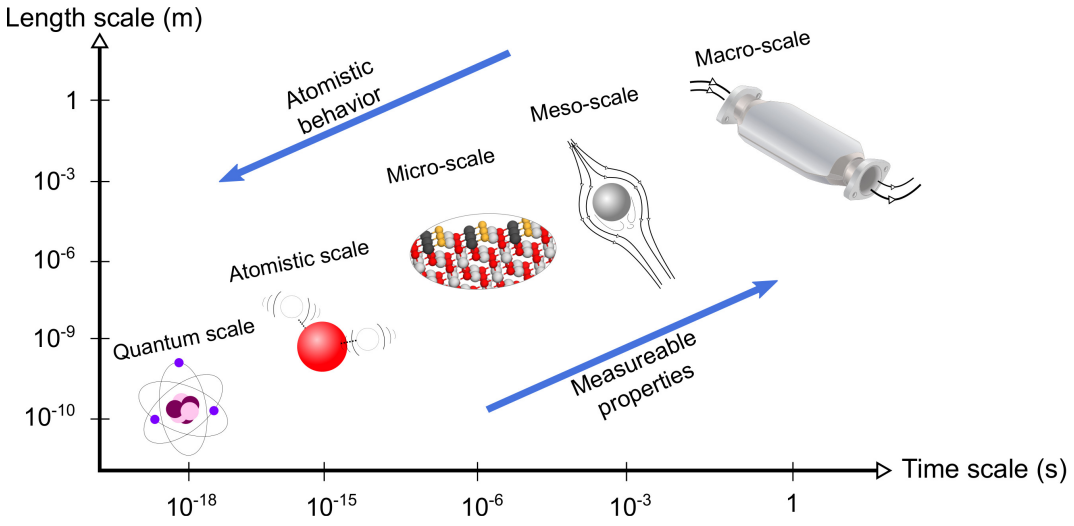

Figure 3.1: Different time and length scales in a heterogeneous catalytic system.

by a feasible method that obtains a solution within a reasonable amount of time. This challenge makes multiscale modelling complex and requires significant computational effort. However, the last decade has revealed many developments with faster computers and more efficient computational methods.

3.1.1 Bridging theory and experiments

There are two main categories of multiscale modelling, the sequential and the concurrent method. In short, these relate to how the infrastructure and the flow of information between the different scales in the model should be handled. In sequential multiscale modelling, the different scales are solved separately and the results are passed upwards in the hierarchy to obtain a final solution. The sequential method is a straight-forward approach and can be used when the different length scales are weakly coupled [85–87]. In concurrent multiscale modelling, the different scales are solved simultaneously, commonly within sub-domains characterized by scales and physics. The two approaches are illustrated in figure 3.2. With the concurrent approach the sub-domains are calculated simultaneously and can be strongly coupled to each other. Hence a smooth transition is desired between the sub-domains since they describe processes at various time and length scales. There are still limitations and challenges to address when using concurrent multiscale models, but once solved the method can be an efficient approach to solve complex problems [85–88].

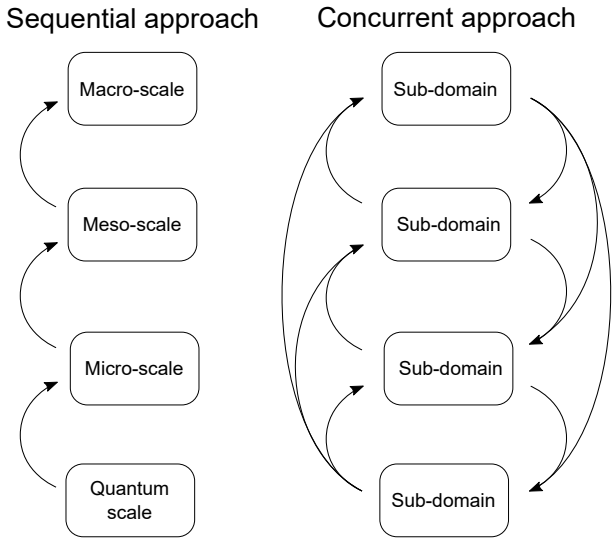

Figure 3.2: Illustration of the sequential and the concurrent approaches to model multiscale systems. The sequential approach passes the results upwards iteratively from the smallest to the largest scale in a straightforward methodology. The concurrent approach passes the results between different sub-domains which are characterised by their scale and physics.

With modern analytical tools the field of surface chemistry has mature to a level where details of the catalyst structure and accurate reactivity data can be determined by *ex situ* and *in situ* methods performed at ultra-high vacuum. However, the conditions ultra-high vacuum can be far from the conditions found in real applications where the material surface and behaviour at atmospheric pressures can differ significantly. The gaps between the appearance and behaviour of well-defined structures, and the appearance and behaviour of the same in realistic conditions are called the materials and pressure gap, respectively [89–92]. Today, we have acquired methods to model atomistic behaviour and developed detailed techniques to monitor the reaction surfaces *in situ* and operando, but yet lack a feasible way of describing the results obtained in one comprehensive multiscale model.

The complexities of multiscale modelling

Developing a comprehensive multiscale model includes several challenges that need to be addressed [93–96]. From the theoretical point of view, clearly defined surfaces are required to describe the kinetics of surface reactions. Even though this is a strength, it is experimentally challenging to manufacture a catalytic structure that contains the exact surface as used by the model. Furthermore, in a prepared catalyst sample, several different surfaces are usually present on the active metal particle due to geometrical differences originating from the manufacturing process, but also at the interfaces between the active metal and metal-oxide support. The different surfaces can show different behaviors and reactivity towards, e.g., methane dissociation. Hence, an inherent complexity exists between the theory and experiments where a challenge remains to examine the same material surfaces. A theoretical approach benefits from detailed and accurate predictions of atomic behavior which difficult to reproduce experimentally. On the other hand, the prepared catalyst surfaces can experimentally show a time-dependent behavior and change its structure due to processes, such as sintering and agglomeration of the active metal at the meso- to macro-scale. The structural changes in time can affect the surfaces and the rate of reaction and adds complexity to correlate theory to experiments. To reduce the gap between theory and experiments studies have reported ways of implementing spillover processes between the active sites and support structure [97–99] and mass and heat transport [96, 100, 101] through first-principles calculations in a heterogeneous catalytic system, but have not yet shown many implementations into a multiscale system. The latter is probably due to the quickly increasing complexity and computational cost. An extensive number of experimental studies [39, 42, 43, 46] have shown that different metal-oxide support materials have a substantial effect on

the observed reaction rate of methane oxidation but few theoretical studies have been published that elucidate support effects on the catalytic cycle [102, 103]. Another complexity of multiscale modelling arises from coupling the different scales present in both experiments and theory. From the quantum mechanical calculations up to the macro-scale of fluid dynamics, they treat vastly different length and time scales, as illustrated in figure 3.1. How to relate between them is a challenging matter in both theory and experiments. When performing experimental measurements it is difficult to fully exclude the effects of time on the material structures at the macro-scale, but also at the smaller scales such as stress and strain of nanoparticles [71]. The complexity of multiscale modelling thus arises from the challenge of treating the events at different scales, by theory and experiments, and whether they are comparable or not.

Avoiding the trap of over-complicating the computational model

In the early development phase of a multiscale model it is tempting to apply the sequential multiscale model approach, owing to its straight-forward structure. In this approach, results are iteratively passed upwards in the hierarchical structure of scales until a converged solution has been found. If this would be done for each time step and if the different scales were to be dependent on each other, the multiscale model would become ineffective and the computational time required to be immense due to the high number of required iterations. Hence, we must make simplifications and do so without sacrificing crucial information about the system. In this work, the single most efficient method would arguably be to decouple some chosen parts of the computational methodology, which can either be calculated in parallel with the main solver or be calculated in advance. To give an example of the latter, one can pre-compute a multi-dimentional array of reaction rates where each dimension corresponds to a reaction condition. This requires that the range of each reaction condition, such as catalyst temperature and partial pressures of reactants and products, is known in advance. The matrix is then called by the main solver in each iteration. One should remember that the common assumptions made in chemical engineering, such as isothermal behaviour and lumping of parameters, are powerful as long as they do not sacrifice the sought information. The question of 'what information is relevant and to what degree of detail?', must be kept in mind.

Recent advancements

The tradition in chemical engineering to develop models has been to describe systems at the macro-scale. The models are usually developed by a power-rate law assumption which includes fitting parameters later to be fitted to experimental data. Empirical

models benefit from accurate model predictions at low computational cost but lack a physical meaning and are only valid for a limited range of reaction conditions. The opposite to empirical models are the first-principles based quantum mechanical models and Dirac wrote in 1929 that the whole of chemistry is completely known from these physical laws [104]. The difficulty is, again, that it leads into a situation where the mathematical expressions are too complicated to solve. During the last couple of decades many advancements in the computational technology have emerged. Not only have models become more detailed thanks to gained knowledge and faster computers, theoretical frameworks and methodologies of how to relate to a multiscale problem have been discussed and themed issues have been released on the topic [105–108]. We are surrounded by multiscale problems but few are today approached as such. Multiscale methods reported in literature have, in general, been developed individually and tailored for specific applications. Since the main difficulty in all multiscale problems is the same, namely the vast flow of information, a general methodological environment could help in further development of multiscale models.

If the matter is given attention, a multiscale model can pave the way for a new and comprehensive possibility of analyzing the catalytic system within heterogeneous catalysis. A model where the reaction rates are based on first-principle calculations at the atomic scale can be used to identify crucial information about the reaction network. During the last decade, studies focusing on methane abatement applications have successfully incorporated comprehensive kinetic models to describe detailed behaviour of the active site and deactivation effects [32, 33, 109]. Furthermore, if mass and heat transport are considered at the macroscopic scale the model can be used to identify limiting factors externally of the catalyst surface (see figure 2.2). Reactor models can also be used to design optimization procedures where, for example, one recent study concluded that an uneven catalyst loading can both improve the activity and reduce the deactivation effect through aging [110]. This mean that multiscale models in the near future can be used to develop concepts and aid catalyst design.

3.1.2 Micro-kinetic reaction rate

To obtain the reaction rates by first-principles calculation one must first determine the energy levels of adsorbed molecules. The energy levels can be determined by density functional theory [111, 112], which has become a common and powerful tool in applied quantum physics to describe reactions. Using density functional theory, a reaction landscape is modelled onto which molecules can adsorb and react. Possible molecular arrangements are identified and their energy levels on the surface are determined. The

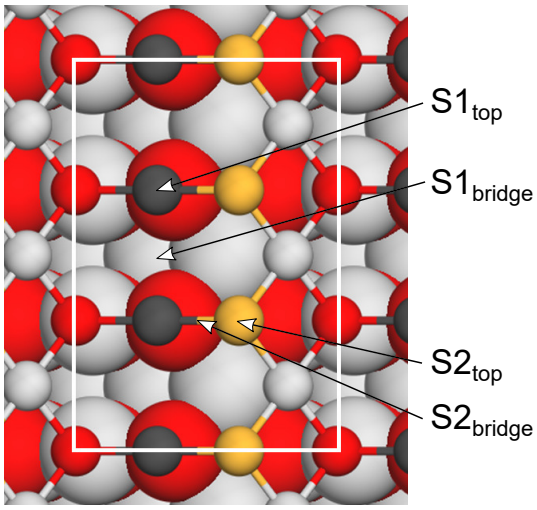

Figure 3.3: The structure of the PdO(101) surface with arrows indicating the different adsorption locations. S1 and S2 denote adsorption on palladium and oxygen, respectively. Adsorption events are possible at a top or a bridged configuration for each surface atom. Atoms in the top-most layer are visualised with smaller balls for clarity. The white box indicates the surface unit cell. Black is a threefold coordinated Pd, yellow is a threefold coordinated O while gray and red are the fourfold coordinated arrangements of Pd and O, respectively.

energy levels are used to calculate the electronic energy barriers for the possible reaction steps as a function of reaction coordinate. Figure 3.3 shows the reaction landscape of the PdO(101) unit surface with corresponding adsorptions sites, which is used in this work.

Transition state theory is a method used to obtain reaction rates between reactants, surface intermediates and products for a micro-kinetic reaction network. Transition state theory (TST) assumes that a reaction step between reactant state (R) and product state (P) progresses through a transition state ($TS^{\ddagger}$), which lies at a saddle point on the energy landscape between the states R and P [113, 114]. The reaction is illustrated as

$$R \longleftrightarrow TS^{\ddagger} \rightarrow P \tag{3.1}$$

Equilibrium is assumed between R and $TS^{\ddagger}$, and the transition between $TS^{\ddagger}$ and P is assumed to be irreversible. According to TST, the rate of which P is produced, k_{TST}, can be expressed as

$$k_{TST} = \frac{k_B T}{h} \frac{Z^{\ddagger\prime}}{Z^R} e^{\frac{-\Delta E}{k_B T}} \tag{3.2}$$

where k_b is Boltzmann's constant, h is Planck's constant, T is the temperature, ΔE is the electronic energy barrier between $TS^{\ddagger}$ and R, and Z^R denotes the partition function for the reactant state. $Z^{\ddagger\prime}$ is the partition for the transition state excluding the reaction

coordinate. The partition functions can be written as a product of the separable partition functions of translational, rotational and vibrational energies which are for clarity shown below. The vibrational frequencies are often obtained through a harmonic oscillation approximation and calculated from the DFT method

$$Z_{trans} = V(\frac{2\pi M k_B T}{h^2})^{3/2} \tag{3.3}$$

$$Z_{rot} = \frac{1}{\sigma}(\frac{8\pi^2 k_B T}{h^2})^{3/2}\sqrt{\pi I_A I_B I_C} \tag{3.4}$$

$$Z_{vib} = \prod_i \frac{e^{-\frac{\hbar\omega_i}{2k_B T}}}{1-\frac{\hbar\omega_i}{2k_B T}} \tag{3.5}$$

where V is the volume of gas, M its mass, σ its symmetry factor, I is the moment of inertia around the axes, $\hbar$=h/2π and ω_i is the vibrational frequency of mode i.

Adsorption events, with the activation energy E_a, are described by the kinetic gas theory and kinetics are described as

$$k_{ads}^{TST} = \frac{S_0 S_{dyn} A_{site}}{\sqrt{2\pi m k_B T}} e^{\frac{-E_a}{k_B T}} \tag{3.6}$$

where S_0 is the sticking coefficient and accounts for the entropy change upon adsorption, S_{dyn} an additional sticking coefficient accounting for the fact that a molecule has to approach the surface in a favorable orientation in order to adsorb, A_{site} is the area per adsorption site and m is the mass of the molecule.

After the temperature dependent rate constants have been determined (equation 3.2 and 3.6), the considered elementary steps are compiled into a reaction mechanism to determine a reaction rate. The reaction rates, as mentioned above, are determined for a single adsorption site. Since the large number of adsorption sites are usually available and that different adsorbates are possible on the adsorption site, a vast number of configurations of adsorbates are existing on the catalyst surface. Hence, numerical calculation of each and every configuration with the effects of the nearest-neighbouring adsorbate is not feasible.

The mean-field approximation assumes that the adsorbates are uniformly distributed over the the surface by saying that (i) there exists a large number of sites, (ii) the surface sites are uniform, (iii) adsorbates diffuse on the surface infinitely fast and (iv) the adsorbate interactions are weak [115, 116]. The approximation allows the reaction rates to be described as mean-field rates where the probability of finding adsorbate *i* on

the surface is equal to the coverage θ. The latter is a common descriptor in experimental catalysis to describe reaction rates. Since strong attractive forces between several adsorbates are present on the surface for oxidation of methane, the mean-field approximation does not make a sufficient prediction of the surface coverages. This is countered by a dividing the relevant adsorbates into paired and unpaired species, where a paired configuration of two adsorbates feel the attractive forces of each other. The paring reactions are assumed to be in thermal equilibrium.

To determine the mean-field rates, take the following reaction as an example where reactant A_2 and B are converted into product C.

$$A_2(g) + B(g) \longleftrightarrow C(g) \tag{3.7}$$

Assume the reaction proceeds via a Langmuir–Hinshelwood mechanism, where the reactants are first adsorbed onto neighboring sites before the surface reaction occurs. The elementary steps of the reaction are written as

$$A_2(g) + 2* \ \longleftrightarrow \ 2A^* \tag{a}$$

$$B(g) + * \ \longleftrightarrow \ B^* \tag{b}$$

$$A^* + B^* \ \longrightarrow \ C(g) + 2* \tag{c}$$

Then the time dependent coverage of surface species A and B are expressed as

$$\frac{\partial \Theta_A}{\partial t} = 2k_a^+ \Theta_*^2 - 2k_a^- \Theta_A^2 - k_c^+ \Theta_A \Theta_B \tag{3.8}$$

$$\frac{\partial \Theta_B}{\partial t} = k_b^+ \Theta_* - k_b^- \Theta_B - k_c^+ \Theta_A \Theta_B \tag{3.9}$$

where Θ_i is the coverage of species i, $k_j^{\pm}$ is the rate constant for elementary reaction j and $*$ denotes a free active site. Equations 3.8-3.9 can be solved numerically to obtain a steady-state solution by letting the left hand side of the equations be zero. For a large number of elementary steps, a general expression can be formulated by the same procedure as

$$\frac{\partial \Theta_i(t)}{\partial t} = \sum_i (\nu_{ij} r_i(\Theta_1, ..., \Theta_N)) \tag{3.10}$$

where $\Theta_i(t)$ is the coverage of surface species i at time t and ν_{ij} is the stoichiometric coefficient for species i and reaction j. Equation 3.10 is solved for steady state mean-field rates and coverages. The obtained mean-field rates are used in the multiscale model at each given gas condition and temperature.

3.1.3 Flow-reactor simulations

Emission control systems, which are the main interest here, are best described as a continuous flow reactor and a monolithic structure is commonly used in both industrial applications and laboratory measurements. Throughout this work, a plug-flow reactor (PFR) is used to describe the molecular dynamics at the macroscopic scale. The channel geometry is representing a monolith with 400 cpsi. The monolith structure is evenly coated with the Pd/Al_2O_3 catalyst. In a PFR the axial dispersion is assumed negligible and the 'tanks-in-series' method is used to discretize the reactor in its length dimension. Tanks-in-series assumes each reactor segment to behave as an ideal tank reactor and thus all fluid properties are uniform within each tank. The evenly coated catalyst is similarly discretized into sublayers to account for internal gradients in the porous catalyst.

Design equations

The mass balance for the bulk gas phase for component *i* is described as

$$\frac{F_{tot}}{A_c} \cdot \frac{dy_{i,g}}{dx} - a \cdot k_{c,i} \cdot C_{tot} \cdot (y_{i,g} - y_{i,s}) = 0 \tag{3.11}$$

where F_{tot} is the total bulk molar flow rate, A_c is the cross sectional area of the porous catalyst, a is the ratio of channel surface area to channel volume, $k_{c,i}$ is the mass transport coefficient of component i and C_{tot} is the total gas phase concentration for the bulk gas. $y_{i,g}$ and $y_{i,s}$ are the mole fractions of component i in the bulk gas and at the porous catalyst surface, respectively. The heat transport in axial direction is described as

$$\frac{F_{tot}C_p}{A_c} \cdot \frac{dT_g}{dx} - h_k \cdot a \cdot (T_g - T_s) = 0 \tag{3.12}$$

where C_p is the heat capacity of the bulk gas, T_g is the bulk gas temperature, T_s is the catalyst surface temperature and h_k is the heat transport coefficient.

The mass balance for component *i* inside the porous catalyst is described as

$$D_{eff,i} \cdot C_{tot} \cdot \frac{d^2 y_{i,s}}{dz^2} + \nu_i \cdot C_{site} \cdot \rho_{cat} \cdot r(C_s, T_s) = 0 \tag{3.13}$$

with boundary conditions as

$$k_{c,i} \cdot C_{tot} \cdot (y_{i,g} - y_{i,s}) = D_{eff,i} \cdot C_{tot} \cdot \left.\frac{dy_{i,s}}{dz}\right|_{z=0} \tag{3.14}$$

$$0 = \left.\frac{dy_{i,s}}{dz}\right|_{z=L_{wc}} \tag{3.15}$$

where ν_i denotes the stoichiometric coefficient for component i, C_{site} is the active site density, ρ_{cat} is the density of the porous catalyst, r is the reaction rate determined from first-principles based microkinetics and L_{wc} is the thickness of the porous catalyst. No mass transport proceeds between the porous catalyst and the cordierite monolith substrate, hence the derivative is set to zero at z=L_{wc} in Eq. 3.15. In accordance to Anderson's criterion [117], the porous catalyst is assumed to be isothermal in radial direction. Thus, the generated heat from the exothermic oxidation reaction is transported from the catalyst surface at a temperature of T_s to the bulk gas phase at a temperature of T_g, or conducted axially through the solid material. The heat balance of the porous catalyst is described as

$$h_k \cdot A_s \cdot (T_g - T_s) - (-2\lambda_s) \cdot A_{cs} \cdot \frac{dT_s}{dx} + \frac{\int_{z=0}^{z=L_{wc}} \rho_{cat} \cdot C_{site} \cdot (-\Delta H_r) \cdot r(C_s, T_s) \cdot dz}{L_{wc}} = 0 \tag{3.16}$$

with boundary condition as

$$-2\lambda_s \cdot \left.\frac{dT_s}{dx}\right|_{z=0,L_{monolith}} = \epsilon \cdot \sigma \cdot (T_s^4 - T_g^4) \tag{3.17}$$

where A_s is the ratio of external surface area to volume of the porous catalyst, A_{cs} is the ratio of cross sectional area to volume of the porous catalyst, λ_s is the catalyst heat conductivity, ΔH_r is the reaction enthalpy, $L_{monolith}$ is the monolith length, ϵ is the emissivity factor (set to 0.6) and σ is the Stefan-Boltzmann constant. The discretized forms of Eq. 3.11-3.17 that were used in the computations are for clarity outlined in the appendix.

Mass and heat transport

The mass (k_c in equation 3.11) and heat (h in equation 3.12) transport coefficients are affected by the flow characteristics (i.e. laminar or turbulent flow) which in turn can affect the rate of reaction [118]. In a turbulent flow the molecular dynamics, and thus the mass and heat transport, are faster compared to in a corresponding laminar flow. Several approaches can be used to calculate the transport coefficients. An interesting, but computationally expensive method, is to incorporate computational fluid dynamics (CFD) to solve the Navier-Stokes equations [119]. CFD is commonly used to track the development of a flow field inside a predefined control volume. Apart from being computationally expensive, to model a porous catalyst with CFD, each pore has to be

predefined. Since the preparation of metal-oxide catalysts usually is performed with a low control of the exact pore structure, CFD can arguably over-complicate the system instead of benefiting towards a reliable solution. However, in emission control system applications, the same type of honeycomb monolith structures have frequently been used in industrial R&D and academic research. Thanks to this, empirical methods of calculating the transport coefficients have been developed over the years. These methods use dimensionless numbers which relate fluid properties to each other in a well-known system. The dimensionless Sherwood and Nusselt number can be used to calculate the mass and heat transport coefficient, respectively. In a fully developed laminar flow, the Sherwood and Nusselt numbers have converged to their asymptotic values of 2.98 [120]. In a monolith reactor geometry, the laminar flow field is least developed in the first part of the monolith which increases the transport coefficients in that area. As the laminar fluid profile develops through the monolith, the Sherwood and Nusselt numbers converge to their asympthotic values. From the asymptotic value, the Hawthorn's correlations can be used to determine the mass and heat transport coefficients between the bulk gas and the catalyst surface as [121].

$$k_{c,i} = Sh_a \cdot \frac{D_i}{dh} \cdot (1 + \frac{0.095 \cdot Re \cdot Sc \cdot dh}{x})^{0.45} \tag{3.18}$$

$$h_k = Nu_a \cdot \frac{\lambda_g}{dh} \cdot (1 + \frac{0.095 \cdot Re \cdot Pr \cdot dh}{x})^{0.45} \tag{3.19}$$

where dh is the open channel diameter, Re is the Reynold number, Sc is the Schmidt number, Pr is the Prandtl number and x is the axial position in the monolith.

The internal diffusion is estimated by the effective diffusivity, $D_{eff,i,k}$. The effective diffusion is estimated from the Bosanquet relation

$$D_{eff,i,k} = \frac{\epsilon_p/\tau}{\frac{1}{D_{i,k}} + \frac{1}{Dk_{i,k}}} \tag{3.20}$$

where ϵ_p/τ is the porosity to tortuosity ratio and set to 0.1 [122, 123]. $D_{i,k}$ is the temperature and total pressure corrected bulk diffusion coefficient and $Dk_{i,k}$ is the Knudsen diffusion coefficient for component i and tank k. $Dk_{i,k}$ includes the structural parameter of pore width. The diffusion coefficients are calculated as

$$D_i = D_{ref,i}(\frac{T_s}{T_{ref}})^{1.75}(\frac{P_{ref}}{P_{tot}}) \tag{3.21}$$

$$Dk_i = \frac{d_p}{3}\sqrt{\frac{8R_gT_s}{M_i\pi}} \tag{3.22}$$

where T_s is the catalyst surface temperature, d_p is the pore diameter, $D_{ref,i}$ is taken from literature values and M_i is the molecular mass of component i.

3.2 Sample preparation

The Pd/Al_2O_3 powder catalyst is prepared by incipient wetness impregnation, also known as dry impregnation or pore volume impregnation. The preparation process requires a predetermined saturation point of water since the volume of added precursor solution should be equal to or less than the total pore volume. This technique is commonly used at larger scale due to its straightforward procedure and when the catalyst precursor is expensive [124, 125]. The alumina support material is impregnated with a palladium salt precursor solution, tetraamminepalladium(II)nitrate, to obtain a desired noble-metal loading of the final catalyst. In practice, prior to impregnation the alumina support is treated in air at 600 °C to remove impurities and its saturation point is determined. The saturation point is determined by drop-wise adding water onto the alumina support material of a known weight. Water is added until the pores of the support material have absorbed their maximum volume and the outer surface turns wet. Once the saturation point is known, a dry sample of the support material is drop-wise impregnated by a prepared aqueous volume of metal precursor, water and ethanol. The resulting paste is instantly frozen with liquid nitrogen and freeze-dried over night to remove the water-ethanol mixture and to deposit the noble-metal on the surface of the support material. The preparation is finalised by calcining the dried powder samples in air at 600 °C for 30 min.

The prepared powder catalysts were washcoated onto monoliths in **Paper I** (L=15 mm, ∅=12 mm) and **Paper IV** (L= 20 mm, ∅=14 mm) and evaluated in a flow-reactor. Prior to the washcoating procedure, the monolith substrate was treated in air at 600 °C for 2 h, the powder catalyst and a suitable binding agent, here Boehmite (AlOOH), was suspended at a ratio of 4:1 in a mixture of water and ethanol (ratio of 1:1). The monolith ends were immersed in the slurry and carefully shaken to remove the excess slurry in the channels to avoid clogging before dried under a heating gun at 100 °C and subsequently calcined at 500 °C for 2 min. This procedure was repeated until the desired mass of catalyst had been applied onto the corderite monolith substrate. The monolith was finally calcined in air at 600 °C for 2 h. The preparation procedure is illustrated in figure 3.4.

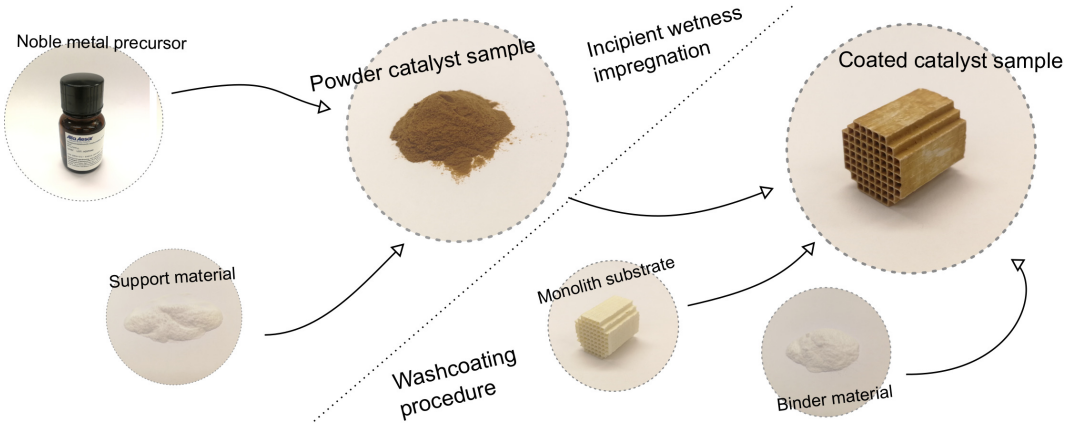

Figure 3.4: A simple flow diagram showing the components in the sample catalyst preparation procedure according to the incipient wetness impregnation and the wash-coating methods.

3.3 Characterisation techniques

3.3.1 Nitrogen physisorption

An inert probing gas can be used to quantify the specific surface area of a mesoporous sample. The theory was first published in 1938 by Stephen Brunauer, Paul Hugh Emmett, and Edward Teller (the BET method) [126]. Nitrogen is commonly used as the inert probing gas which physisorbs onto the solid surface. The BET method assumes (i) equilibrium between the adsorbate and the solid surface, (ii) the physisorption sites are equivalent in the first layer of adsorbate, (iii) molecules in N^{th} layer act as physisorption sites for layer N+1, (iv) adsorbate-adsorbate interactions are neglected, (v) the adsorption is described equally for layers N$\geq$2, (vi) the adsorption energy for layer N$\geq$2 is equal to the condensation energy of the probe gas and (vii) the number of layers become infinite at P=P_0 where the adsorbate condenses into a liquid on the solid surface [127].

To measure the surface area of a mesoporous sample, the sample is dried before being cooled to the boiling point of the liquid nitrogen (-196 °C). The cooled sample is evacuated and in steps dosed with small volumes of nitrogen where the pressure is allowed to stabilize before the consecutive dose. The amount of nitrogen physisorbed onto the sample (V) is measured as a function of the relative pressure of P/P_0, where P is the equilibrated partial pressure and P_0 is the saturation vapour pressure of nitrogen at -196 °C. At low partial pressures, the relationship between physisorbed nitrogen and partial pressure is linear and the monolayer volume (V_m) is determined by the slope, $(C-1)/V_mC$, and intersection, $1/V_mC$, between $0.05 \leq P/P_0 \leq 0.3$, according to the BET

equation 3.23 [126]. The surface area is quantified from V_m and the cross-sectional area of the N_2 molecule (0.162 nm^2).

$$\frac{P}{V(P_0 - P)} = \frac{C-1}{V_m C}\frac{P}{P_0} + \frac{1}{V_m C} \tag{3.23}$$

The pore size distribution (PSD) of mesoporous materials can be calculated by a method originally proposed by Barrett *et al.* [128]. The approach assumes a step-wise emptying of the pores, which are assumed to initially be filled with condensed N_2 at a relative pressure of close to unity. Capillary condensate is removed from the pores along with the step-wise desorption process where the largest pores are assumed to be emptied before the narrower pores due to a smaller surface tension. Using the relative pressure and the Kelvin equation, which uses surface tension to relate the relative pressure to pore size, the PSD and an average pore width can be calculated. The method is a simplified description of the actual occurring process and contains errors but is recognised as a standard method to determine PSD in mesoporous materials.

The surface area and average pore size of the catalyst samples used in **Paper I** and **Paper IV** were measured in a Micromeritics TriStar 3000 instrument.

3.3.2 Selective chemisorption

Selective carbon monoxide chemisorption is a method which can measure the dispersion of e.g. noble metals in a known catalyst sample. The dispersion is defined as the ratio between exposed metal atoms and the total number of atoms of the considered metal in the sample. In the procedure, the sample was first degassed at 250 °C for 3 h to remove surface moisture and to determine its dry weight. After the dry weight was determined, the sample was subjected to an oxidative pretreatment of 2 vol.-% O_2 at 500 °C for 1 h followed by a reductive pretreatment, 4 vol.-% H_2, at 500 °C for 1 h. The pretreatment procedure enables the exposed metal atoms to chemisorb carbon monoxide. The sample is cooled to 35 °C before carefully dosed with carbon monoxide. By monitoring the number of chemisorbed carbon monoxide molecules and assuming a ratio of adsorbed CO per metal atom, the metal dispersion can be determined.

In **Paper I** and **Paper IV**, the dispersion of Pd and the mean Pd particle diameter were determined by chemisorption of carbon monoxide using a Micrometrics ASAP 2020 instrument.

3.3.3 Diffusive reflectance infrared Fourier transform spectroscopy

Infrared (IR) spectroscopy is an important technique in research to measure molecular vibrations by creating a change in the dipole moment. A commonly used analytical tool in catalyst research is diffuse reflectance infrared Fourier transform spectroscopy (DRIFTS), which can be used to study powder samples and solids with a rough surface. The technique is based on the interaction between the IR radiation and the vibrational modes of the chemical bonds in a molecule. The emitted IR radiation consists a range of frequencies which can excite different vibrational modes of equivalent energy. The vibrational modes may be associated with bending, vibration or rotation of the molecular bonds [129]. The vibrational modes of a bond is dependent on the atom mass at each end of the bond, and the bond strength. The latter is in turn affected by adjacent molecular structures. This results in that the vibrational modes in a molecular system are unique and hence can be used to identify the surface species and the functional groups present on the sample surface. DRIFTS was used in **Paper IV** to identify surface species adsorbed on the Pd/Al_2O_3 surface.

3.4 Catalyst evaluation

3.4.1 Flow-reactor measurements

Two different flow-reactor systems were used to evaluate the performance of the prepared catalysts. In **Paper I**, where elevated total pressures were examined, an in-house built flow-reactor of stainless steel was used that can withstand the increased force exerted on the material. The flow-reactor was designed to operate in parallel, but not simultaneously, with a diffusive reflectance infrared Fourier transform spectroscopy instrument (Vertex 80v). The parallel setup enables a quick change from kinetic measurements to surface characterisation and uses the same gas delivery system. In the flow-reactor, the coated monolith sample is surrounded with quartz wool and fixed in an insulated stainless steel tube (L=480 mm, $\varnothing_O$=15 mm). An electrical heating coil is fixed onto the stainless steel tube and positioned directly upstream of the coated monolith sample to ensure a reliable feed gas temperature. The heating coil is controlled by a Eurotherm 3216 temperature controller. The feed gas temperature is measured by a K-type thermocouple 5 mm upstream of the coated monolith and mass flow controllers (Bronkhorst model FG-201CV) are used to deliver the desired gas composition. The total pressure is measured by an in-line mounted gauge pressure transmitter (Yokogama, model EJA530E) and controlled by a control valve (Bronkhorst F-001). The gas delivery, system pressure and temperature are controlled and monotored in a LabVIEW environment. The gas outlet is analysed by mass spectroscopy (V&F Analysetechnik,

Airsense Compact). Prior to each experiment, the sample underwent a pretreatment procedure. In **Paper I**, where pressureised conditions are tested, the sample was pretreated at 500 °C with 4 vol.-% H_2 for 20 min and with 2 vol.-% O_2 for 40 min before cooled to 280 °C in 2 vol.-% O_2 and Ar. The pretreatment procedure and the consecutive activity measurement was carried out at the same total pressure and at a total flow of 100 mL min^{-1}. The activity measurements were conducted by increasing the temperature with 2 °C/min up to 450 °C, held constant for 30 min followed by a cooling phase with 2 °C/min. The methane conversion was calculated from the cooling phase of the measurement. The apparent activation energies were calculated using data points between 7 and 15 % methane conversion. The reaction orders were determined by varying the concentration of methane between 400 and 1600 vol.-ppm in steps of 200 vol.-ppm with unchanged temperature and pressure.

In **Paper IV** a similar flow-reactor setup was used to measure the activity of the catalyst. This flow-reactor consists of an insulated quartz tube which is surrounded by a heating coil. K-type thermocouples are placed in front of and inside the monolith sample to measure the feed gas and sample temperature, respectvely. Gas delivery is handled by mass flow controllers (Bronkhorst model FG-201CV) controlled by a LabVIEW environment. The outlet gas concentration is measured by FTIR Spectroscopy (MultiGas 2030, MKS Instruments). The pretreatment procedure in **Paper IV** included five consecutive ignition-extinction temperature ramps to reach a steady-sate performance of the sample. The ignition-extinction ramps where performed at subsequent reaction gas composition of either a dry (0.1 vol.% CH_4 + 2 vol.% O_2) or a wet (0.1 vol.% CH_4 + 2 vol.% O_2 + 5 vol.% H_2O) gas feed. The temperature was increased by 4 °C/min from 200 to 500 °C where it was held constant for 5 min before decreased to 200 °C with 4°C/min.

3.4.2 Simulations

Paper I-**IV** discuss the simulated catalytic activities to assess the catalytic performance at elevated pressures and discuss the applicability of the multiscale model. The input parameters required by the model are monolith dimensions, catalyst mass, noble-metal loading, palladium dispersion, feed gas temperature, gas composition, total pressure and volumetric flow. The simulations assume an even coating of catalyst thickness through the monolith and an even noble-metal distribution in the washcoat except in **Paper III** where an additional simulation with an uneven noble metal distribution was performed.

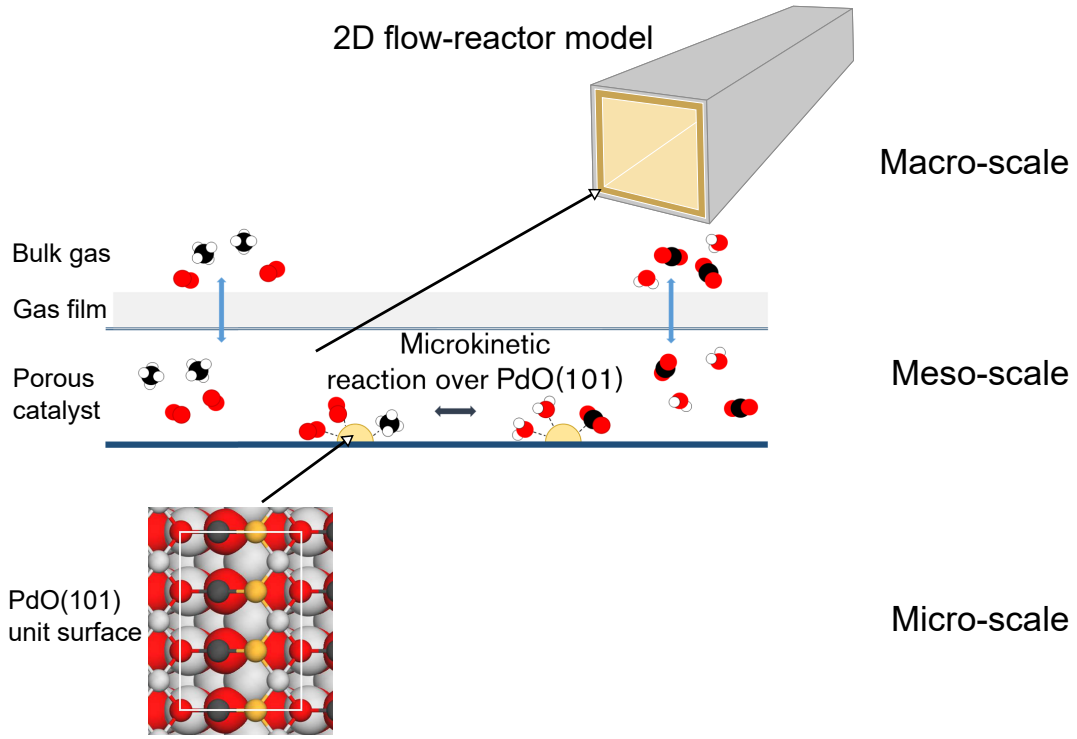

Figure 3.5: An illustration of the 2D multiscale model.

The mass and heat transport equations for the bulk gas phase (equation 3.11 and 3.12) and for the porous catalyst (equation 3.13 and 3.16) are coupled to the first-principles based microkinetic reaction rate in equation 3.10. The reactor is discretised into tanks and catalyst sublayers, which are solved numerically in order to obtain axial and radial gradients. The monolith is simulated as a single-channel reactor. The single-channel monolith is divided into 10 tanks, according to the tanks-in-series method, while the porous catalyst is divided into 12 sublayers to account for internal mass and heat transport. The length of the tanks and the thickness of the sublayers increases with 30 % from the inlet and 50 % from the catalyst surface, respectively, to obtain a finer gradient resolution. An illustration of the reactor model is shown in Figure 3.5. The active site density, c_{site}, is determined from a desired palladium loading and dispersion in each tank and sublayers. The active site density is calculated in each tank and sublayers to obtain the predetermined site distribution inside the catalyst. The coated catalyst is given the physical properties of alumina. The simulations are performed using a combination of MATLAB and the Python software. The macroscopic calculations of molecular flow dynamics through the monolith and into the catalyst structure are calculated in MATLAB environment while the microkinetic calculations are calculated using the SciPy Python package.

CHAPTER 4

COMPLETE METHANE OXIDATION

In this work, the performance of Pd/Al_2O_3 catalysts for complete methane oxidation at varying total pressure has been studied by experiments and simulations in dry conditions, and simulated for wet exhaust gas compositions. The performance in pressurised atmospheres, lean (oxygen excess) and dry conditions is studied by activity measurements using an in-house built flow-reactor, which has been designed and constructed as a part of this work. The activity measurements are accompanied by simulations using a 2D multiscale flow-reactor model which has been developed for the specific purpose as discussed in section 3.1.3. While the main focus is to study the effect of total pressure, comparison between experimental and simulated activities is an interesting addition where first-principles calculations based kinetics are compared to experimentally measured values. The multiscale flow-reactor model is used to evaluate the performance of the Pd/Al_2O_3 catalyst at simulated exhaust gas conditions (5-10 vol.-% H_2O and CO_2). It is known from previous studies that interface sites, located between the noble metal and the supporting metal-oxide structure, may impact the activity of the catalyst. The interface sites are not included in the multiscale model to limit the computational cost without adding fitting parameters. Simulated results from the multiscale flow-reactor model are therefore compared to corresponding experimental results for a series of prepared Pd/Al_2O_3 catalysts with varying ratio of interface to bulk palladium sites to discuss and emphasise the necessity of including support effects. This section discusses the general trends and findings of the results, and focuses on the total pressure effects on the catalytic activity and the possibilities of multiscale modelling in heterogeneous catalysis.

4.1 Pressurised methane oxidation over Pd/Al_2O_3

The study in **Paper I** measures the methane conversion at dry conditions using the in-house build flow-reactor as described in section 3.4.1. The methane conversion is measured between 300 and 450 °C and the accompanying simulations use determined noble metal loading and dispersion, measured by inductively coupled plasma-optical emission spectrometry and selective chemisorption, respectively. Figure 4.1 shows that the methane conversion is enhanced with increasing total pressure between the examined temperatures for increasing total pressures, along with an increased activation energy. In the region of lower temperatures, where kinetics are usually controlling a chemical reaction, the methane conversion is more or less unaffected by an increased total pressure. For increasing temperatures, the methane conversion increases faster for the experiments and simulations performed at elevated total pressures. The total pressure effect is thus more pronounced at higher reaction temperatures until a full conversion is achieved. The experiments only show a minor effect of total pressure above 4 atm. The equations used in the multiscale flow-reactor model contain no fitting parameters, and two distinct and different length and time scales are coupled, the first-principles calculations at the atomistic scale for kinetics over PdO(101) and the macroscopic scale for flow dynamics through a monolith reactor. The simulations in figure 4.1 therefore do not consider the effects of support material, structural changes nor

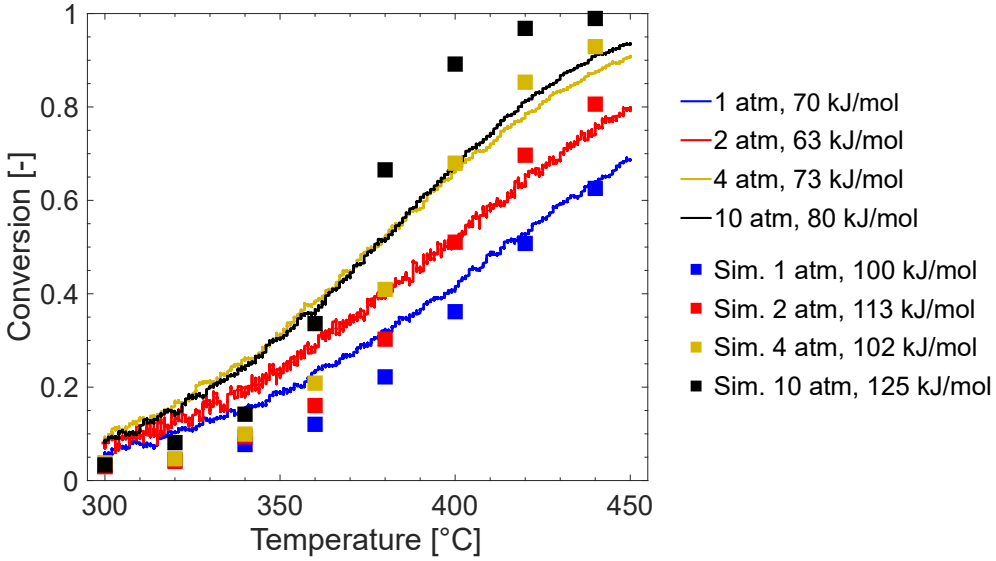

Figure 4.1: Experimental (lines) and simulated methane conversion (squares) at 1 (blue), 2 (red), 4 (yellow) and 10 (black) atm in dry conditions (0.1 vol.-% CH_4 + 2 vol.-% O_2) and activation energies. The gas flow was balanced in Ar with an inlet space velocity of 100 mL min^{-1}, which corresponds to a GHSV of 3500 h^{-1} at atmospheric total pressure.

differentiate between the different active site. Surface area changes of the active sites were successfully implemented by Stotz *et al.* into a similar flow-reactor model, which could partly explain the differences seen in this work [33]. The effects of support material and structural changes inevitable during the experiments but the present model manages to capture the general experimental trends with a some exceptions. One exception is the diminishing total pressure effect above 4 atm which is not observed in the simulated activity profiles. Another is the underestimated simulated activity at low temperatures. The study in **Paper I** discusses other possibilities than structural changes of the active sites, which also can have an effect on the methane conversion within the examined temperature range. These can crudely be categorised as effects on transport properties and effects on the reaction kinetics. **Paper I** concludes that the observed effect of increasing total pressure as shown in figure 4.1 is attributed to a sufficiently high fraction of under-coordinated palladium sites, a longer residence time for the methane inside the catalyst coated monolith, due to fixed inlet mass flow, and a higher methane impingement rate.

4.1.1 Effects on transport properties

The total pressure effects on the transport properties in **Paper I** are studied. The bulk molecular diffusion is affected by the total pressure and decreases linearly as described by equation 3.21. A decreasing bulk diffusion in turn affects the effective diffusion for the internal mass transport considerations and the mass transport coefficient for gas film (external) diffusion shown equations 3.20 and 3.18, respectively. In the prevailing conditions of (0.1 vol.-% CH_4 + 2 vol.-% O_2) the internal mass transport can be assumed to influence the observed rate of reaction at atmospheric pressures and temperatures of 450 °C as discussed in **Paper I**. The significance of internal mass transport is estimated by the Weisz modulus (Ψ) and shown in figure 4.2. It might be surprising that the internal mass transport is most influential at atmospheric and not at elevated total pressures, since a higher methane conversion was observed and a slower diffusion is expected at the latter. The suspicion is motivated and the question is touched upon in **Paper II-III** where higher temperatures are studied. At this point, in **Paper I**, the methane reaction rate is slow and an increased total pressure reduces the concentration gradients inside the porous catalyst, hence reducing the influence of internal mass transport. The influence of temperature and total pressure on bulk diffusivity, Knudsen diffusivity, effective diffusivity and the mass transport coefficient for methane are shown in figure 4.3 at inlet conditions according to the multiscale model. It is observed that the Knudsen diffusion is between one and two orders of magnitude lower than the bulk diffusion and hence impacts the effective internal diffusion (D_{eff}) according

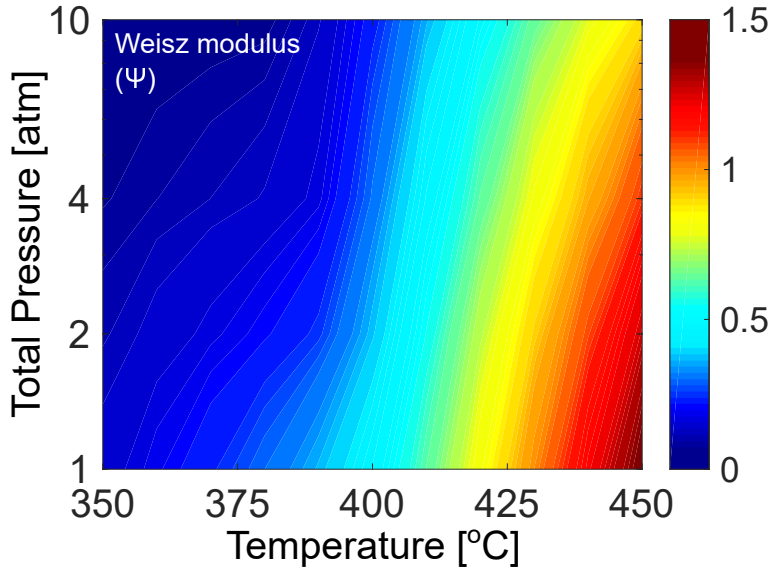

Figure 4.2: The Weisz modulus calculated at experimental inlet conditions for varying total pressures and temperatures. An average catalyst coating of 30 μm is estimated from optical microscopy while the reaction rate and effective diffusivity is taken from the multiscale model. Values are taken from the multiscale model since differential conditions can not be assumed at all examined conditions.

to the Bosanquet relation in equation 3.20. The external mass transport is found to be insignificant according to the Mears criterion and the effects on heat transport can be assumed negligible for all examined conditions in **Paper I**. The results indicate that the methane oxidation is most likely controlled by a mixture of kinetics and internal mass transport in dry conditions since $\Psi \sim 1$.

4.1.2 Effects on methane reaction rate

The effects of total pressure on the intrinsic reaction rate of methane in **Paper I** can be estimated by the microkinetics in the multiscale model. The total pressure is raised at maintained reactant concentrations to explain the observed positive effect. However, a few words about the reaction network are first necessary. The microkinetic reaction network is based on a dual-site mechanism, where under-coordinated palladium and an under-coordinated oxygen atom is required for methane dissociation. Examining the fraction of unoccupied palladium, S_1(Pd), and oxygen, S_2(O), sites displays a high availability of S_1(Pd) sites and a low availability of oxygen sites in dry conditions. Thus a low availability of S_2(O) sites is indicated to be limiting the methane oxidation reaction. Studying the adsorbates reveals that hydrogen is abundant on the the S_2(O) sites which is formed through the CH_x decomposition reaction. The fraction of available S_2(O) sites and the coverage of hydrogen are shown in figure 4.4. At temperatures where a low methane conversion is observed in figure 4.1, a high coverage of hydrogen is pre-

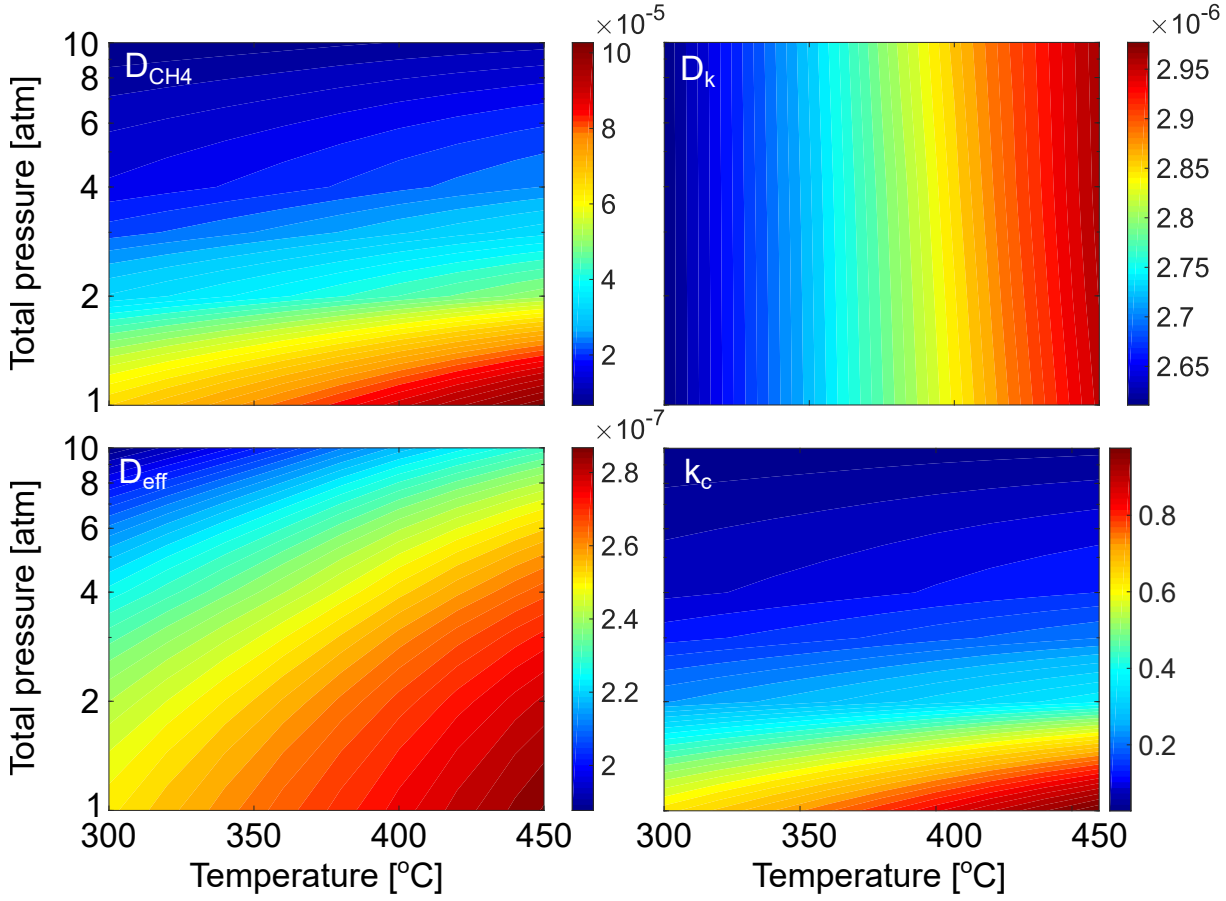

Figure 4.3: The bulk molecular diffusion (a), Knudsen diffusion (b) and the effective diffusivity (c) for CH_4 at inlet conditions according to the multiscale model.

dicted by the simulations which is enforced by studies that report a high rate-control of the methane dissociation and the CH_3 decomposition reaction step of methane oxidation over palladium [77,130]. Further, the observation of a limiting fraction of available $S_2(O)$ sites at temperatures where the simulated methane conversion is under-estimated is interesting since the observation could indicate and point towards the necessity of including support effects to the model and explain the overestimated simulated activation energies. The support effects could very well influence the availability of $S_2(O)$ sites or the surface reactivity itself through interface sites, oxygen storage capacity and other regeneration pathways for the $S_2(O)$ sites. Including such information into the multiscale model could enhance the kinetics at low temperatures and take the multiscale model one step closer to the results from corresponding experiments. Indications that the effects of support material should be considered have been reported in a similar study [33].

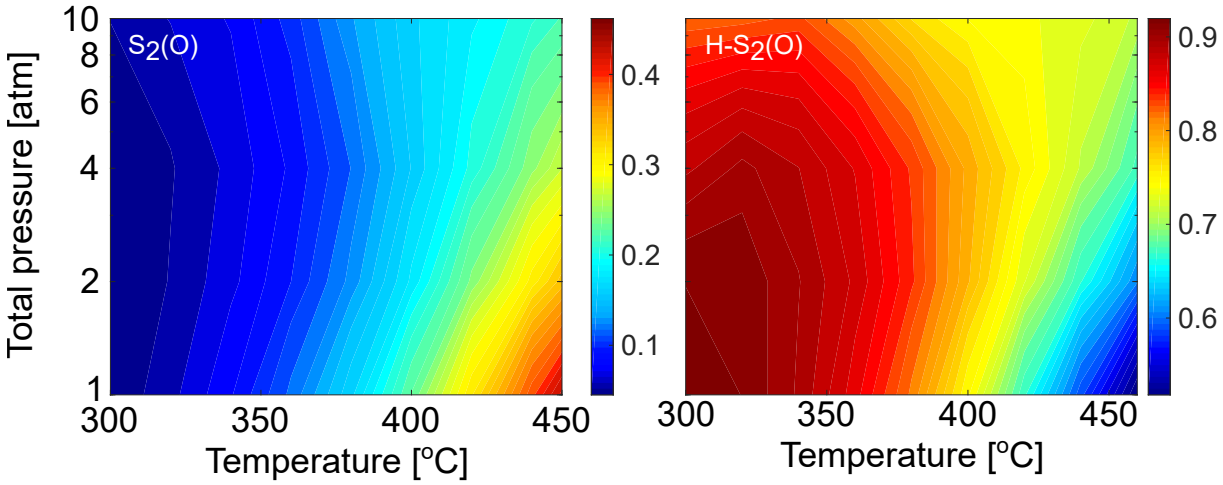

Figure 4.4: The fraction of unoccupied under-coordinated oxygen sites (left) and the coverage of adsorbed hydrogen on the $S_2(O)$ site (right) at varying temperatures and total pressures according to the microkinetic model.

4.2 Simulated activity at exhaust gas conditions

The model is used in **Paper II** and **Paper III** to predict the behaviour of a similar Pd/Al_2O_3 catalyst at realistic exhaust gas conditions where also water and carbon dioxide are present in the feed gas. The concentrations vary but usually 5-10 vol.-% of each component is present in a real application. In **Paper II** the axial dimension in the 2D flow-reactor model is removed and a differential length segment of the reactor is analysed at inlet reactor conditions. Thus, no bulk gas flow is present and steady-state turnover frequencies are simulated in radial direction inside the coated catalyst. The 2D multiscale model is reintroduced in section 4.2.3 and **Paper III** to evaluate the flow-reactor performance at simulated exhaust gas conditions.

4.2.1 Intrinsic reaction rate

The temperature and total pressure dependent turnover frequencies in **Paper II** are shown in figure 4.5. In contrast to the previously discussed results of **Paper I** where dry conditions are used, **Paper II** displays that the turnover frequency can be negatively affected for simulated exhaust gas conditions. A negative effect of total pressure is observed below temperatures of 420 °C while a positive effect is present above 475 °C. Between 420 and 475 °C the effect of total pressure is low but a temperature and total pressure dependent local maximum in the turnover frequency is observed. The three temperature regions with different dependency of total pressure on the turnover frequency are from here on called the low-, intermediate- and the high-temperature regime. The study in **Paper II** reveals that the origin of the three temperature regimes

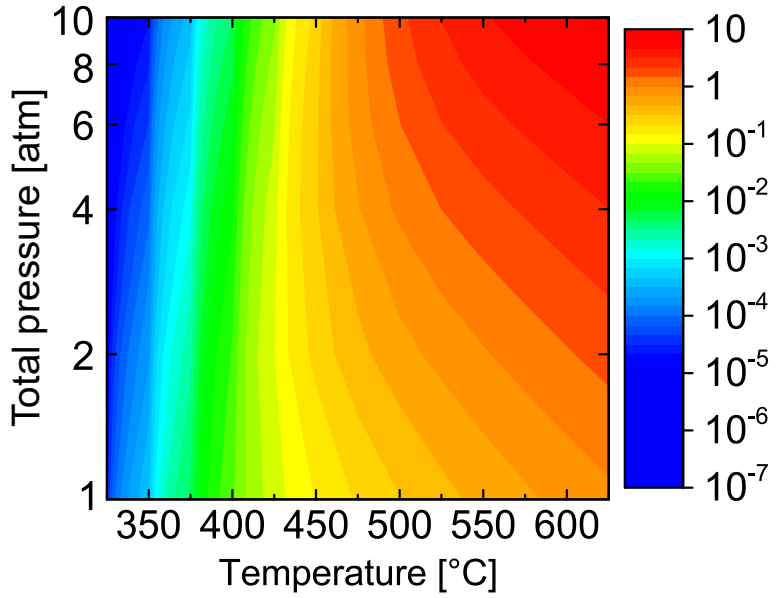

Figure 4.5: Simulated intrinsic turnover frequencies for complete methane oxidation over a Pd/Al_2O_3 catalyst at varying temperature and total pressure. The simulated exhaust gas is comprised of 0.1 vol.-% CH_4, 10 vol.-% O_2, 5 vol.-% H_2O and 5 vol.-% CO_2.

are due to temperature and total pressure dependant coverages of the most abundant surface intermediates on the palladium and oxygen sites, S_1(Pd)-S_2(O). An analysis of the surface adsorbates reveals that the S_1(Pd) sites are blocked by adsorbed bicarbonate (HCO_3), water and hydroxyl species (OH). The reduced number of available S_1(Pd) sites results in a lower chance of finding an available S_1(Pd) site next to an available S_2(O) site, which is the most reactive configuration of adsorption sites for methane dissociation on the PdO(101) surface. The adsorbate coverages, and the chance of finding an available S_1(Pd)-S_2(O) site configuration, are shown in Figure 4.6a-d. The bicarbonate species is formed from a surface reaction between adsorbed carbon dioxide and hydroxyl species while the hydroxyl species originates from decomposition of adsorbed water or as a reaction intermediate from decomposition of adsorbed CH_x species. The negative effect of increased total pressure on methane conversion in the low-temperature regime is explained by an increasing coverage of hindering surface species on the under-coordinated S_1(Pd) sites. Bicarbonate is found to dominate the Pd/Al_2O_3 site surface at temperatures up to ∼400 °C while adsorbed water and hydroxyl species are favoured between 400-450 °C and the observed negative effect is hence a combination of these two. Interestingly, a possible interplay between the carbon dioxide and water, and their negative effects on the reaction rate was previously observed and discussed experimentally [34, 131]. For temperatures within the high-temperature regime, the fraction of available S_1(Pd)-S_2(O) site configurations is sufficiently high to

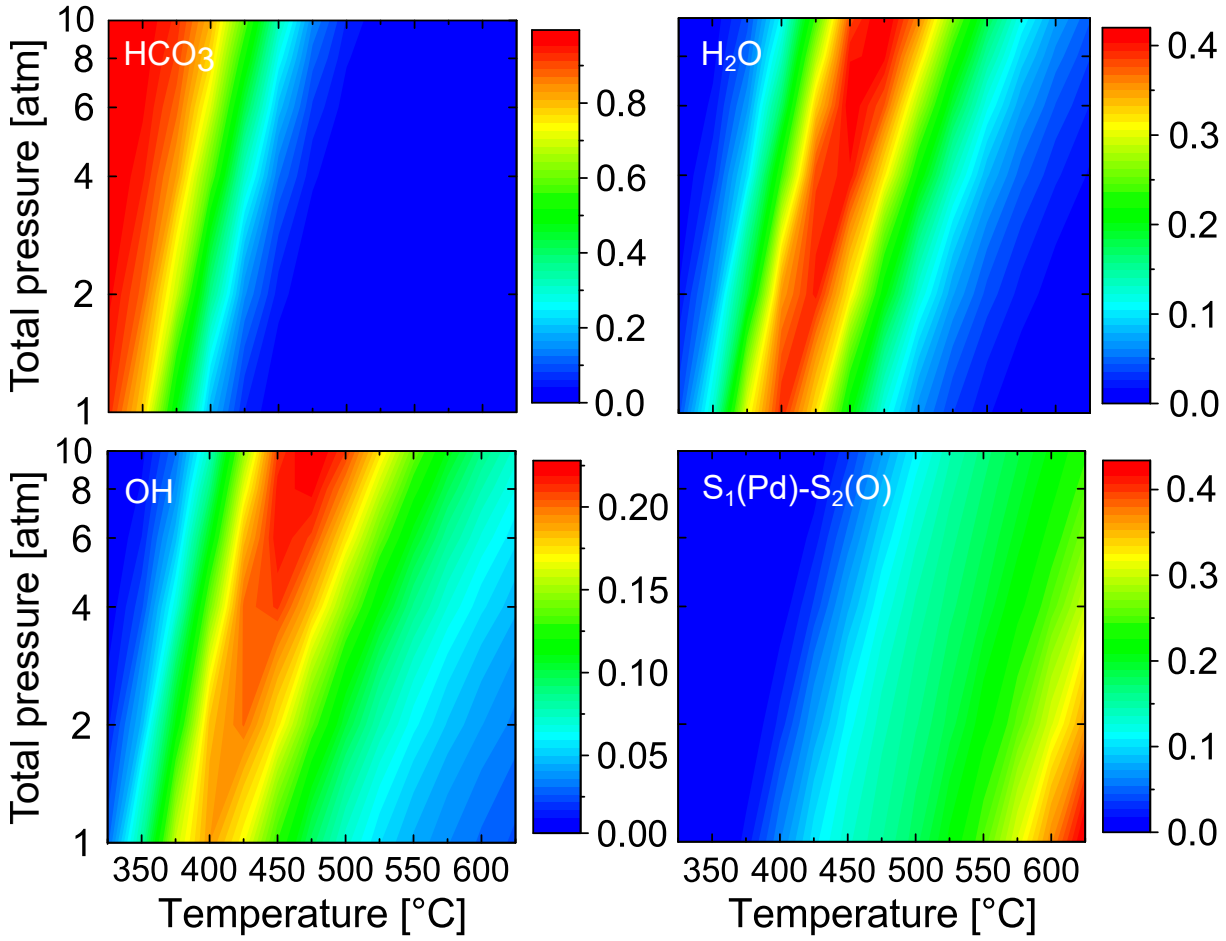

Figure 4.6: The equilibrium coverages of bicarbonate, water, hydroxyl species and the fraction of available S_1(Pd)-S_2(O) site configurations according to the microkinetic model. The bulk gas is comprised of 0.1 vol.-% CH_4, 10 vol.-% O_2, 5 vol.-% H_2O and 5 vol.-% CO_2.

dissociatively adsorb the methane molecule when the total pressure is increased. The availability is relatively high even at the highest examined total pressure which explains the observed positive effect of total pressure. The main findings of the study in **Paper II** are the three temperature regimes with different total pressure dependencies and the explanation is found in the adsorbed surface species which are blocking the under-coordinate palladium site, S_1(Pd), in the S_1(Pd)-S_2(O) site configuration.

4.2.2 Mass and heat transport effects

So far, section 4.2 has treated intrinsic turnover frequencies by giving the mass (k_c) and heat (h_k) transport coefficients and the effective diffusivity (D_{eff}) large values. From this point on, the values are determined according to the transport equations in section 3.1.3. The turnover frequencies in figure 4.5 are recalculated at the same reaction conditions to obtain simulated mass and heat transport affected turnover frequencies.

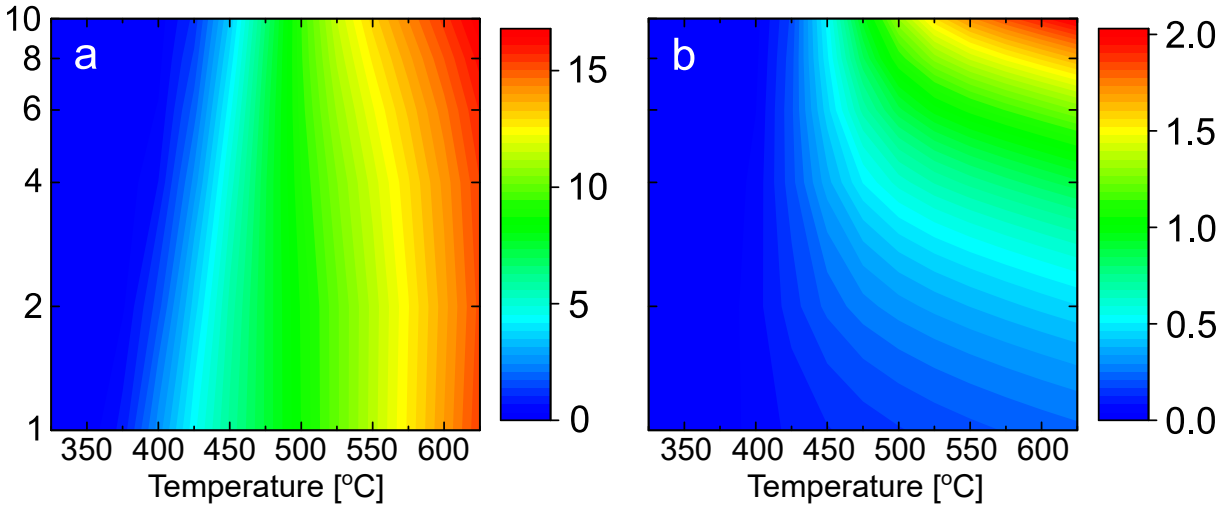

Figure 4.7: The significance of internal (a) and external (b) mass transport for complete methane oxidation in a Pd/Al_2O_3 washcoat at varying temperature and total pressure. The simulated exhaust gas is comprised of 0.1 vol.-% CH_4, 10 vol.-% O_2, 5 vol.-% H_2O and 5 vol.-% CO_2.

For the sake of simplicity, the 'simulated mass and heat transport affected turnover frequencies' will from here on be denoted just as 'turnover frequencies'. The internal and the external mass transport significance are evaluated by comparing the their diffusion time constants (t_{wc} and t_d, respectively) to the reaction time constant (t_r). In the case of internal mass transport significance, the ratio of t_{wc}/t_r coincides with the Weisz modulus and for the external mass transport significance, the ratio t_d/t_r is analogous to the Mears' criterion. Their significance are shown in figure 4.7. In accordance with **Paper I**, the internal mass transport in figure 4.7a begins to influence the turnover frequencies around 400 °C where the significance is close to unity. However, in the high-temperature regime an increasing significance is noticed for increasing total pressure. This effect was not displayed in **Paper I** and the difference between figure 4.2 and figure 4.7a is that the latter examines higher temperatures. At temperatures above ∼500 °C the fraction of available S_1(Pd)-S_2(O) site configurations is high and the turnover frequency can increase unhindered with increasing total pressure, giving rise to internal concentration gradients of methane and an increased internal mass transport limitations. The external mass transport significance in figure 4.7b indicates that external mass transport can be neglected in the low-temperature regime (T<420 °C).

By defining a criterion saying; if one time constant is an order of magnitude higher than the other (e.g. $t_{wc}/t_r \geq 10$), the process described by the highest time constant can safely be assumed to control the reaction rate of methane. The simulated turnover frequency with determined controlling regions are shown in figure 4.8. The criteria show

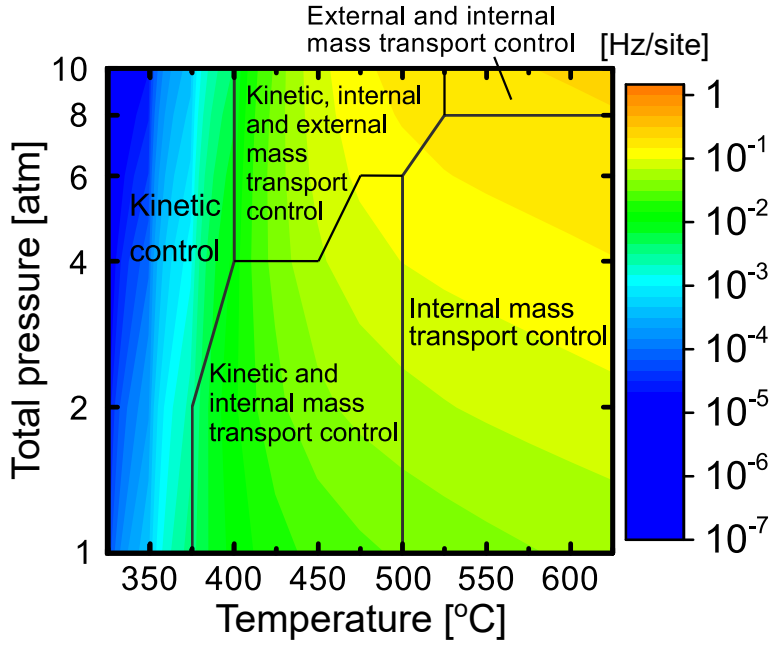

Figure 4.8: The volume averaged simulated turnover frequencies with determined controlling regions in the Pd/Al_2O_3 catalyst for methane oxidation at varying temperature and total pressure. The simulated exhaust gas is comprised of 0.1 vol.-% CH_4, 10 vol.-% O_2, 5 vol.-% H_2O and 5 vol.-% CO_2.

that the reaction rate of methane oxidation, in a simulated exhaust gas composition and in a Pd/Al_2O_3 coated monolith, can be assumed to be kinetically controlled at temperatures below ~400 °C. In the kinetically controlled region the turnover frequency is determined by the number of available S_1(Pd)-S_2(O) site configurations, which in turn are low due to a high coverage of bicarbonate, water and hydroxyl species. The high coverage results in a hindering effect for dissociative methane adsorption on the S_1(Pd)-S_2(O) site configuration. Internal mass transport influences come into play above ~400 °C and the external mass transport is shown to influence but never control the reaction at high temperatures, as discussed in more detail in **Paper II**.

4.2.3 Reactor performance

The study in **Paper III** explores the performance of a flow-reactor according to the 2D multiscale flow-reactor model and predicts methane conversion profiles at simulated exhaust gas conditions. The methane conversion profiles in Figure 4.9a put the observations in **Paper II**, into context and once again displays three different total pressure dependencies. A negative effect of total pressure on the methane conversion is noticed at the lower temperatures, here up to 420 °C while a positive effect is seen above 450 °C. The cause for the observed effects is as in **Paper II**, found in the temperature and total pressure dependent surface coverages of bicarbonate, water and hydroxyl species

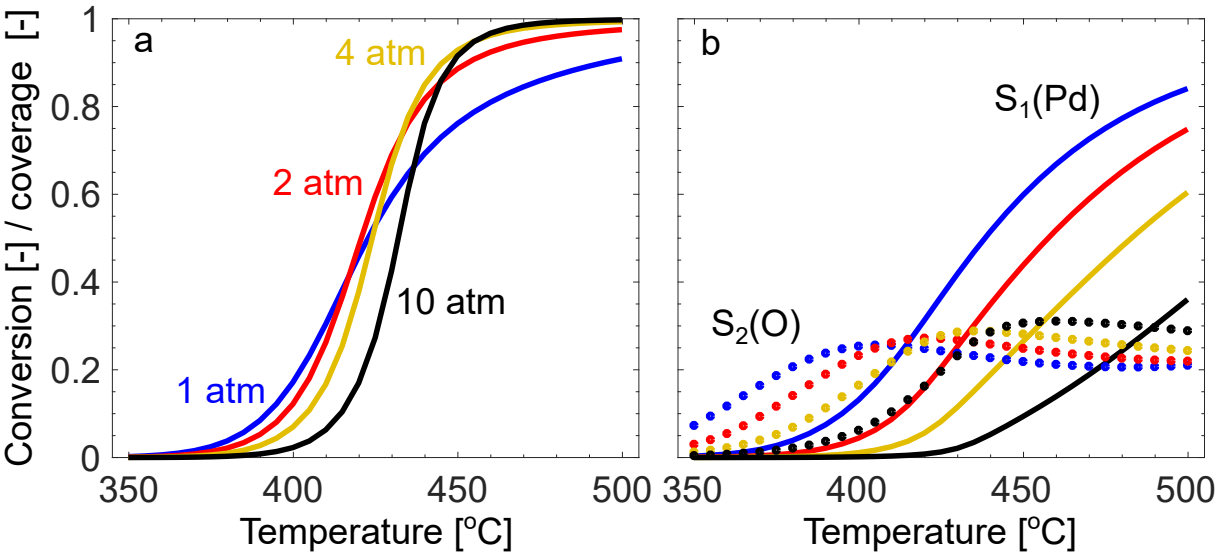

Figure 4.9: The simulated methane conversion profiles (a) with the corresponding fraction of available S_1(Pd) and S_2(O) sites on the palladium oxide surface (b). The simulated exhaust gas is comprised of 0.1 vol.-% CH_4, 10 vol.-% O_2, 10 vol.-% H_2O and 5 vol.-% CO_2 balanced in Ar with an inlet space velocity of 1500 mL min^{-1}. The flow rate corresponds to a GHSV of 53 000 h^{-1}.

that adsorb on the under-coordinated S_1(Pd) sites and hinder methane dissociation. The fraction of available S_1(Pd) and S_2(O) sites are displayed in figure 4.9b. When a negative pressure effect is observed the availability of under-coordinated S_1(Pd) sites is limited by a high coverage of hindering surface species. This is explained by adsorption of gaseous CO_2 and water from the bulk gas and was not observed at the examined dry conditions in **Paper I** where under-coordinated oxygen sites were instead limiting due to a high coverage of hydrogen. The kinetic control of methane oxidation is hence controlled by different kinetic steps that are dependent on the bulk gas composition. This is further complicated by including the total pressure as a variable since the ratio between available S_1(Pd) and S_2(O) sites seems to be highly dependent of both temperature and total pressure (figure 4.9b).

A degree of rate control analysis is performed In **Paper III** for the microkinetic reaction network. The results show a high rate control of the methyl decomposition and water desorption for the surface kinetics in a simulated exhaust gas composition at lower total pressures. The main results from the degree of rate control analysis are shown in figure 4.10. The observed rate control of water desorption is not surprising and the negative effect of water adsorption has already been discussed. Figure 4.10 illustrates this since an unoccupied S_1(Pd) site is formed upon water desorption from the surface. In the methyl decomposition reaction step, a hydrogen species is transferred from the methyl group to either a surface hydroxyl or an under-coordinated oxygen site. Further,

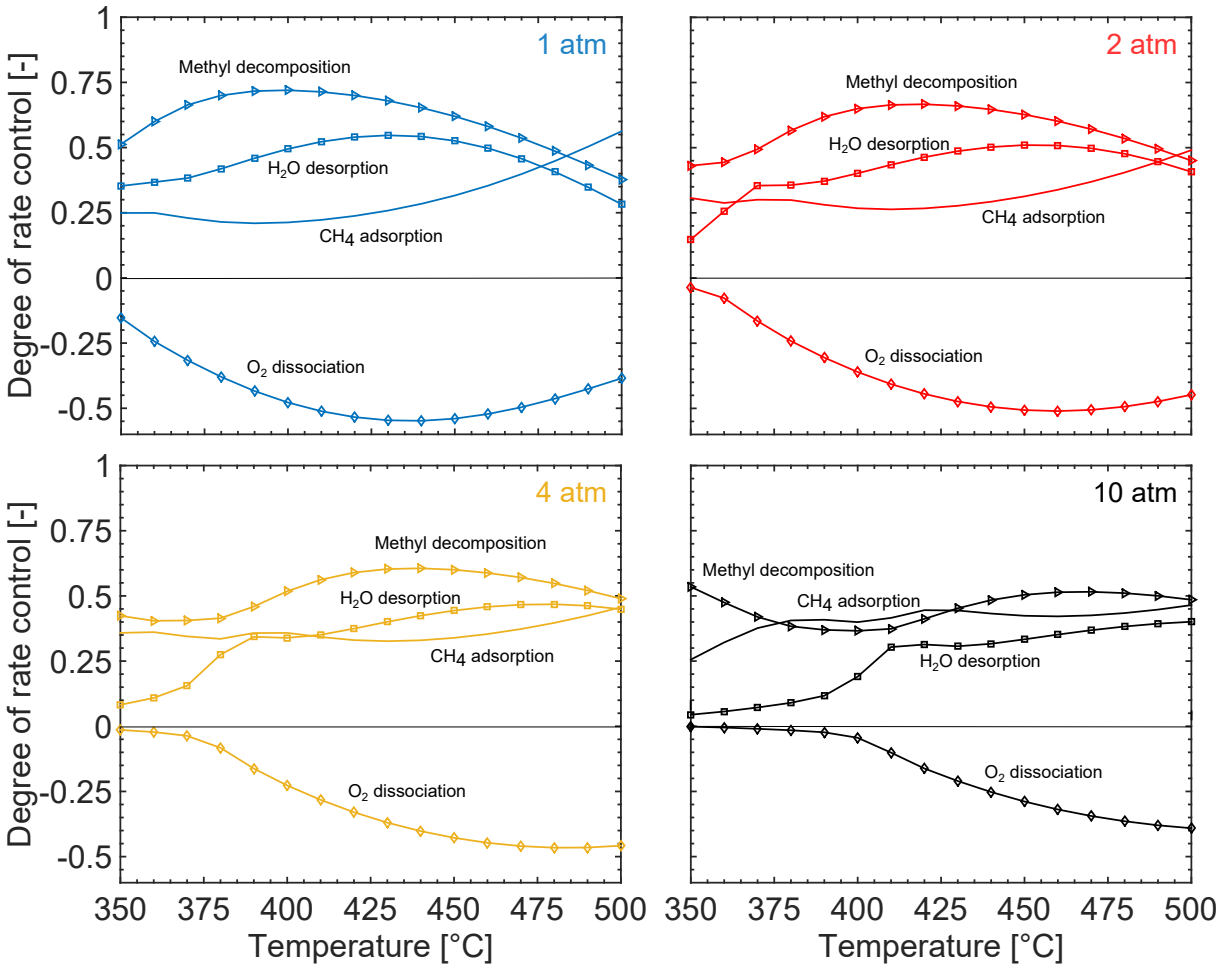

Figure 4.10: The temperature and total pressure dependent degree of rate control determined from simulations at inlet gas conditions of 0.1 vol.-% CH_4, 10 vol.-% O_2, 10 vol.-% H_2O and 5 vol.-% CO_2.

O_2 dissociation shows a strong negative rate control because of the additional S_1(Pd) site the extra oxygen occupies. For increasing total pressures the rate control of methyl decomposition and the water desorption decrease while a more influencing methane adsorption is seen and shows similar rate control for the methane oxidation reaction at 10 atm. The low rate control of water desorption at high pressures and low temperatures is explained by an increased surface coverage of bicarbonate, which becomes favoured over the adsorbed water on the S_1(Pd) sites at higher total pressures. One might be surprised that bicarbonate formation is not revealed in the degree of rate control analysis even though its high surface coverage and effect. The explanation is due to the fact that the elementary step of bicarbonate formation is not part of the reaction cycle. The formation takes part in a parallel, and independent, pathway to form the bicarbonate surface species. This result in a low degree of rate control low but the negative effect of carbon dioxide adsorption, from which bicarbonate is formed, is instead observed as

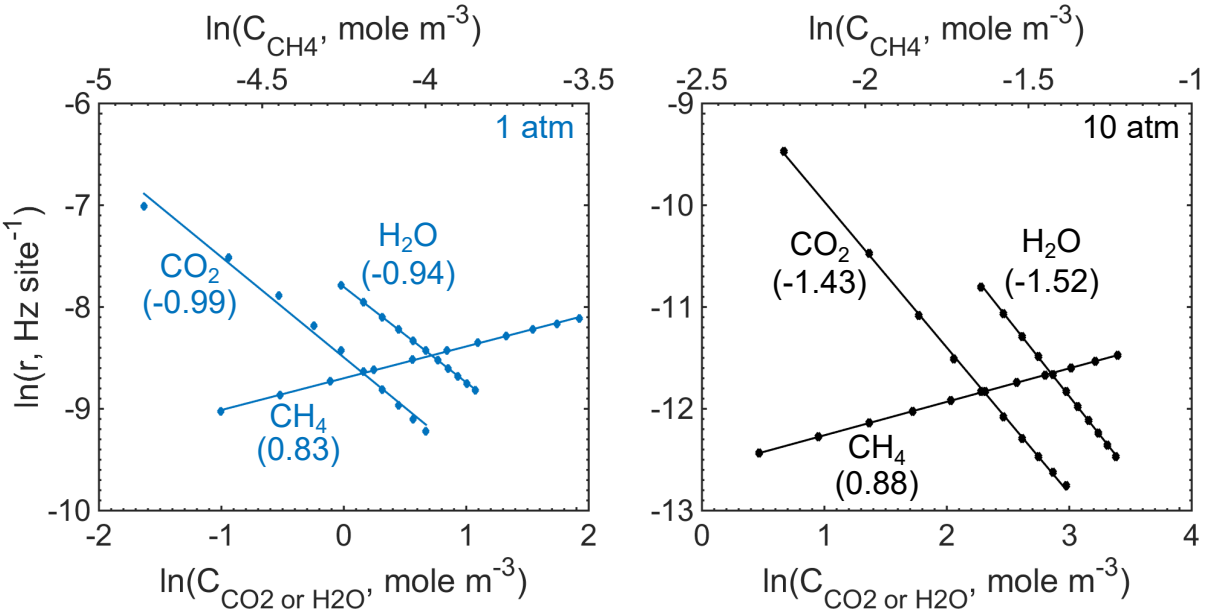

Figure 4.11: Reaction orders for methane, carbon dioxide and water at 1 (blue) and 10 (black) atm. The reaction orders are determined using the 2D multiscale model for a gas composition of 0.1 vol.-% CH_4, 10 vol.-% O_2, 10 vol.-% H_2O and 5 vol.-% CO_2 balanced in Ar at a total inlet flow rate of 1500 mL min^{-1}.

a negative reaction order in **Paper III**. The reaction orders for methane, carbon dioxide and water are determined at 350 °C at 1 and 10 atm and shown in figure 4.11. The reaction orders at 1 atm are similar to previous work [132–134]. Increasing the total pressure is shown to only slightly enhance the methane reaction order. The carbon dioxide and water reaction orders however show a strong negative effect by increasing the total pressure which is attributed to the hindering effect previously discussed. The water adsorbs on S_1(Pd) sites and decomposes into hydroxyl and hydrogen that through several different surface diffusion reactions can end up as hindering species for the methyl decomposition reaction. Adsorbed carbon dioxide forms a carbonate which reacts with a surface hydroxyl to ultimately end up as the hindering bicarbonate surface species.

4.3 Support effects

The low activity of methane oxidation of Pd/Al_2O_3 in a wet feed gas and the resulting effects on the support structure is commonly debated [39, 40, 62, 63, 65]. Since the microkinetics in the multiscale flow-reactor model do not consider supported palladium particles but an ideal surface, it may be of interest to make the comparison between experimental with simulated activities. The discussed adsorbates of water and hydroxyl species in **Paper II-III** are investigated experimentally by diffusive reflectance infrared

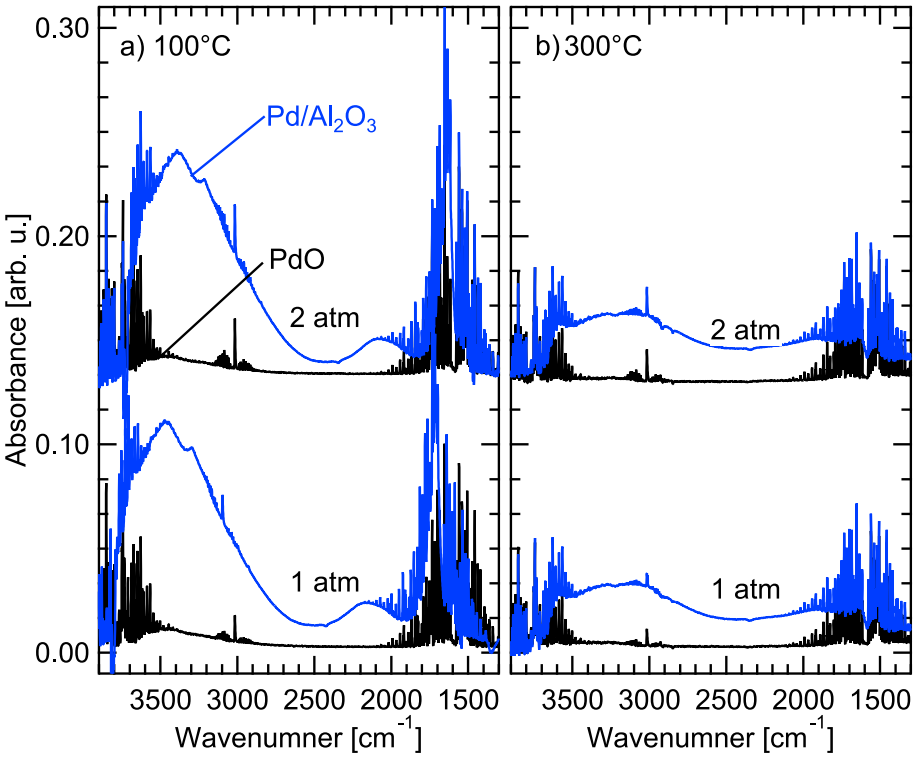

Figure 4.12: Diffusive reflectance infrared Fourier transform spectra during exposure of Pd/Al_2O_3 (blue) and PdO (black) for 0.1 vol.% CH_4 + 10 vol.% H_2O at 100 and 300 °C . The difference spectra were first taken at a total pressure of 1 atm followed by 2 atm.

Fourier transform spectroscopy. The difference spectra at 100 and 300 °C and 1 and 2 atm for powder samples of Pd/Al_2O_3 and unsupported PdO are shown in figure 4.12. Not surprisingly, the spectra show a higher absorbance at 100 °C, compared to 300 °C, in the hydroxyl stretching region above 3000 cm^{-1} due to fewer adsorption events. The difference spectra for the alumina supported and the unsupported palladium oxide powder show a marginal effect of increasing total pressure from 1 to 2 atm, except for a higher gas phase absorbance of CH_4 (3015 cm^{-1}) and H_2O (2000-1400 cm^{-1}). However, the two samples show distinct differences in the hydroxyl stretching region. A relatively high number of adsorbed hydroxyl species is thus present for the Pd/Al_2O_3 sample compared to the unsupported PdO sample. In the former, the hydroxyl species are present on the alumina support [65, 135, 136]. For the unsupported PdO sample, only a small amount of hydroxyl species are observed which are assumed to be adsorbed on the under-coordinated palladium atom, as previously discussed in **Paper II-III**. The observation indicates that there can most likely exist an effect, such as spill-over of hydroxyl species and presence of interface sites, that the simulations do not consider when predicting the methane conversion.

The effects on the support material exerted by a wet feed gas have earlier been investigated by experimentally studies [65, 137–139]. Interestingly, Velin *et al.* concludes that the interface sites, between the palladium oxide particles and the alumina support, seems to be of vital importance for the methane oxidation activity and involved in the observed inhibitory effects of a wet feed gas [65]. The hypothesis that the lack of interface sites in the model can explain the underestimated activity in the multiscale model (figure 4.1), was studied in **Paper IV** at atmospheric total pressure. Two series of catalyst samples were prepared with varying palladium loading and dispersion and their activity for methane oxidation were experimentally measured by the procedure outlined in section 3.4.1. The two catalyst series consists of a parent and a thermally treated series of samples, both originating from the same sample batch. The samples are prepared by incipient wetness impregnation and the thermally treated samples have additionally been calcined to gain similar palladium area as the 0.23 wt.-% Pd/Al_2O_3 parent sample. Through this procedure the samples vary in terms of palladium dispersion and loading, hence also the ratio of bulk palladium to interface palladium atoms. It is here suggested that the ratio of bulk palladium to interface palladium sites can partly describe the results of **Paper IV**. The ratio increases with increasing palladium loading due to an increasing particle size and the bulk palladium would hence be more similar to the PdO(101) surface used in the multiscale model. The methane conversion and corresponding 2D flow-reactor simulations are shown in figure 4.13. The study illustrates and indicates that the multiscale model better predicts the experimentally measured activities for larger particles (higher fraction of bulk palladium sites) in dry conditions. In wet conditions however, the flow-reactor model overestimates the activity which is argued to originate from a lack of spill-over effects from the support, where hydroxyl species migrate from the alumina support to the active palladium sites. Another similar argument arises from the fact that in wet experiments a slow long-term hydrothermal deactivation effect of water is present but not considered by the steady-state simulations. The sintering process reduces the palladium dispersion over time and since the simulations compare a catalysts with fresh properties to pretreated catalysts, an additional loss of activity would be expected. **Paper IV** demonstrates the necessity of including support effects and interface sites to develop a model for supported palladium particles. The added support effects and interface sites should preferably be based on first-principles calculations if we want to enhance our understanding of atomistic behaviour of the palladium supported catalyst.

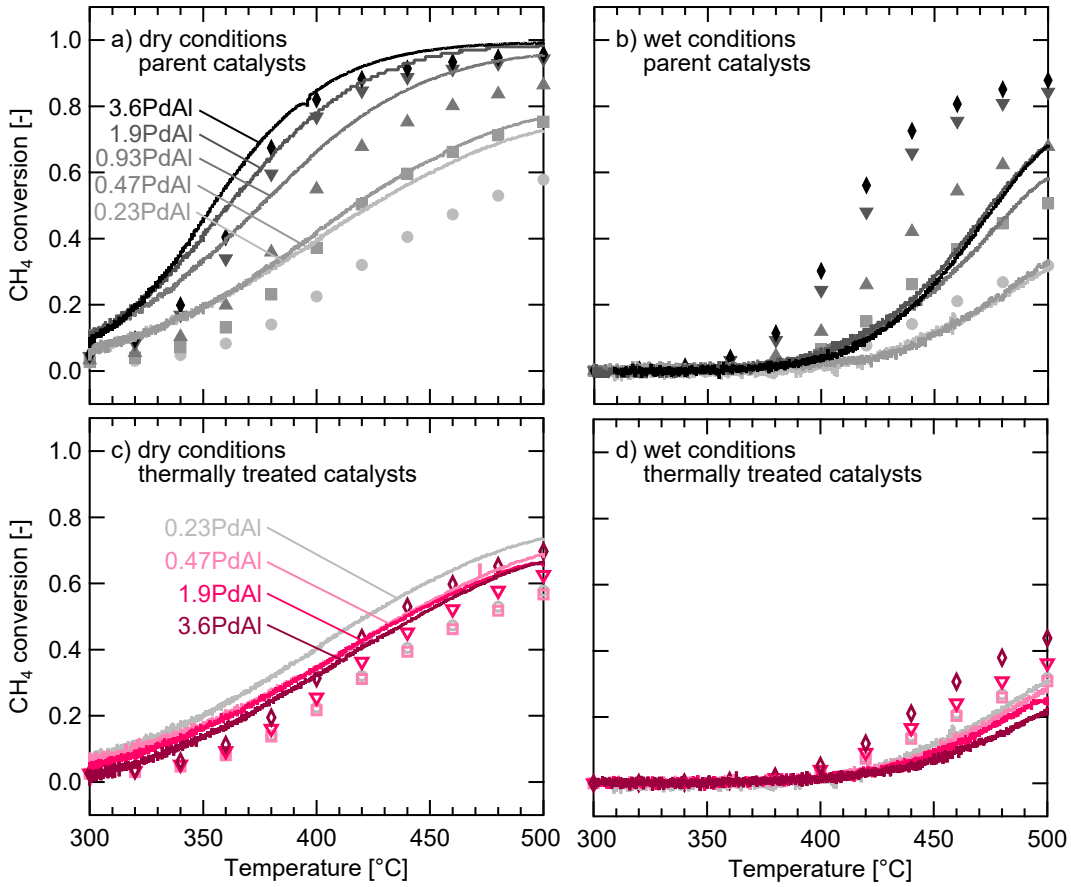

Figure 4.13: Experimental and simulated methane extinction profiles. Top row: parent samples of 0.23, 0.47, 0.93, 1.9 and 3.6 wt.-% Pd/Al_2O_3. Bottom row: Thermally treated samples with similar palladium areas but varied ratios of bulk-to-interface palladium sites. Left column: Dry oxidation of 0.1 % CH_4 in 2 % O_2. Right column: Oxidation of 0.1 vol.-% CH_4 in 2 vol.-% O_2 + 10 vol.-% H_2O.

CHAPTER 5

CONCLUSIONS AND REFLECTIONS

The aim of this thesis is to investigate whether or not an increased total pressure above atmospheric pressure can enhance the methane conversion over an alumina supported palladium catalyst. The work studies the complete methane oxidation reaction and compares experiments and simulations by developing a 2D multiscale flow-reactor model. The studies appended to this thesis conclude that the activity of Pd/Al_2O_3 can be enhanced by raising the total pressure of the system above atmospheric pressure and that the effect is dependent on the feed gas composition and reaction temperature. The results demonstrate that in dry and oxygen rich conditions, the methane conversion along with the apparent activation energy, increases for increasing total pressures. The simulated methane conversions, using the multiscale flow-reactor model, are able to capture the trends of corresponding experiments and are used to explain the differences. The reaction kinetics at the micro-scale of the multiscale model are based on first-principles calculations. The surface reactions occur on palladium oxide in the PdO(101) surface where both the under-coordinated palladium atom and the under-coordinated oxygen atom act as separate adsorption sites. In dry conditions, the Pd/Al_2O_3 catalyst exhibits a high fraction of available palladium sites and is limited by a low fraction of available oxygen sites. The low fraction of available oxygen sites is a result of a high coverage of adsorbed hydrogen, which originates from the successive decomposition of adsorbed methane. The total pressure is shown to exhibit a low effect on the mass and heat transport properties which alone do not explain the effect of total pressure on the reaction rate. For the examined temperatures (300-450 °C) and total pressures (1-10 atm), the observed reaction rate is controlled by a combination of surface kinetics and internal mass transport. When the Pd/Al_2O_3 catalyst is exposed to a simulated exhaust gas composition from combustion of methane (0.1 vol.-% CH_4, 10 vol.-% O_2, 10 vol.-% H_2O

and 5 vol.-% CO_2) the fractions of available palladium and oxygen sites are strongly dependent on the temperature and total pressure. Gas phase water and carbon dioxide in the feed adsorb on the palladium sites and hinder methane dissociation at lower temperatures. The microkinetic reaction network, based on first-principles calculations, predicts a high coverage of adsorbed water, hydroxyl species and bicarbonates where the first two originate from gaseous water and the last one originates from a surface reaction between adsorbed carbon dioxide and hydroxyl species. Hence, at simulated exhaust gas composition a higher temperature is necessary to maintain a positive effect of total pressure in the oxidation of methane. The higher temperature is required for the desorption of hindering surface species to increase the fraction of available palladium sites of the palladium oxide on the catalyst surface. If the temperature is insufficient, an increased total pressure results in an increased coverage of surface species that hinder the reaction and thus a lower catalytic activity due to a slower dissociative adsorption of methane. It is shown that the methyl decomposition has rate control of the catalytic cycle and when the total pressure is increased, the dissociative adsorption of methane becomes more important due to an increased adsorbate competition. The strong negative effects of gas phase water and carbon dioxide are seen as negative reaction orders, which decrease with increasing total pressure.

Comparing experimental activity measurements with multiscale simulations demonstrates the advantages of combining reaction kinetics based on first-principles calculations with commonly used flow-reactor models. Multiscale models will most probably play an important role in the near future to evaluate catalytic systems and to drive the research forwards into finding new catalyst designs and formulations. However, the computational power is still a limiting factor and simplifications and assumptions must be accepted in the computational approach. This work demonstrates that the next step for multiscale models, and using first-principles calculations based methods within heterogeneous catalysis, should target the inclusion of support effects and find feasible methods of doing so.

5.1 Contribution to complete methane oxidation catalysis

At the beginning of this project, the knowledge about the influence of total pressure on the conversion of methane was limited but new studies, at the time, investigated the option of an upstream turbine position of a catalytic abatement system [30, 31]. These studies concluded that the catalyst volume can be reduced if the total pressure

is increased, which is in agreement with the results of the present thesis. One question of interest still remains whether the increased total pressure might in fact be a result of an increased residence time of reactants inside the reactor since the inlet molar flow is kept constant. Therefore, varying the space velocity should be addressed in the future to evaluate if the results are similar, or equal, to a corresponding increased total pressure. At this point, it is indicated that the effect of total pressure on space velocity is important but additional studies should be performed to elucidate whether there exists a synergistic effect of residence time and total pressure on the surface kinetics.

Furthermore, the work has developed and used a multiscale flow-reactor model which was not available from the start of the project. The multiscale flow-reactor model shows that this kind of multiscale modelling is possible by today's standards but is limited by the computational cost. Few similar models have been reported in the area of heterogeneous catalysis but have lately emerged to describe reaction kinetics in detail. The combination of a reaction network based on first-principles calculations coupled to flow-reactor simulations, show great possibilities in understanding reactions from a broader perspective.

5.2 Reflections on the computational approach

As discussed in the beginning of section 3.1, multiscale modelling is today limited by an insufficient computational power to account for all the sub-processes that might be of interest. During the development phase of the present multiscale flow-reactor model this was made clear by an unfeasible computational time required to obtain a solution. Here, the first-principles based microkinetic part of the code was iteratively called in each time step and hence a system of ordinary differential equations (ODEs) at the micro-scale had to be solved within another system of ODEs at the macro-scale. The matter can probably be solved using different strategies and assumptions, but in this work it was decided to assume that the micro-scale does not affect the macro-scale. The assumption allows the reaction kinetics to be decoupled from the mass and heat transport equations and thus the reaction rates can be pre-calculated and combined into a multidimensional array where each dimension corresponds to a reaction parameter. Further, a computer cluster was used to simulate up to twenty experimental conditions at a time. The two rather simple procedures created a computational method which runs over a feasible amount of time. However, convergence issues must also be addressed since the system of ODEs is stiff, especially at conditions resulting in high reaction rates. The solution is eased by first obtaining steady-state simulations for the isothermal case, then slowly ramping up the isothermic heat from zero to true values

to finally obtain the simulated results. Since multiscale models are computationally expensive and assumptions are required, one must choose what information is important for the system and consider to neglect the rest. Preferably one should perform a background study before developing the multiscale model to evaluate what is important and what can be neglected. Once this is done and a multiscale model is developed, one must never forget that even though the reaction kinetics are based on first-principles calculations from density functional theory and transition state theory, errors are probably present at every scale. The user should not accept a multiscale model as the truth which could lead to erroneous conclusions. When errors, however small, are present it can be tough to draw too detailed conclusions on the macro-scale. However, from a conceptual point of view the results should be true and show similar trends, as this multiscale flow-reactor model manages to predict for the studied system.

Acknowledgements

The research was carried out at the Division of Applied Chemistry and the Competence Centre for Catalysis at the Department of Chemistry and Chemical Engineering at Chalmers University of Technology, Göteborg, Sweden during the period October 2015 to January 2020.

The Competence Centre for Catalysis is hosted by Chalmers University of Technology and financially supported by the Swedish Energy Agency and the member companies AB Volvo, ECAPS AB, Johnson Matthey AB, Preem AB, Scania CV AB, Umicore AG & Co. KG, Volvo Car Corporation AB and Wärtsilä Finland Oy.

The research is funded by the Competence Centre for Catalysis. The computational time was granted by SNIC at C3SE (Göteborg).

Additionally I would like to thank:

My main supervisour, Magnus Skoglundh, for your constant support and belief in this project. I appreciate the trust you have give me to take the project in a different direction (probably) than we both though at first. For always welcoming discussions whenever needed and keeping your door open, the friendly atmosphere and fun moments. I have learnt many things thanks to you. Men kom ihåg, ingen minns en fegis.

My co-supervisors Per-Anders Carlsson, Derek Creaser and Henrik Grönbeck. Standing in between chemical engineering and chemical physics would have been a much tougher challenge without your feedback over these years.

My examiner, Hanna Härelind. You are always so positive and it is a pleasure to have you around and I know that you will do great work as our new head of division.

I this work would have a different story if it wasn't for Lasse Urholm, Lennart Norberg and Ulf Stenman. Your work and support in the reactor labs can not be acknowledged enough. Your work help so many of us.

My fellow colleges and friends at TYK and KCK, past and present, for all the coffee and after works we have had. Your friendship have made this time a blast. I will look back and remember the time together with joy. Let's meet up again on the other side.

A special thanks goes to Anna. The last year you have encouraged me, believed in me and help me to keep myself together. It is now my turn to do the same to you. Then, we lift our eyes from the present and walk into the future.

Of course, my family, parents and brother, for your extraordinary support end encouragement over so many years. You taught me to see the positive side of things and "det löser sig alltid, på ett eller annat sätt". Without you I would probably not even have started this journey.

BIBLIOGRAPHY

[1] B. Lindström and L. J. Pettersson, *Cattech*, 2003, **7**(4), 130–138.

[2] E. Fulhame, *An Essay on Combustion, with a View to a New Art of Dying and Painting. Wherein the Phlogistic and Antiphlogistic Hypotheses are Proved Erroneous.*, London : Printed for the author, by J. Cooper, 1794.

[3] K. J. Laidler and A. Cornish-Bowden, in *New Beer in an Old Bottle: Eduard Buchner and the Growth of Biochemical Knowledge*, ed. ed. A. Cornish-Bowden, 1997; chapter Elizabeth Fulhame and the discover of catalysis: 100 years before Buchner, pp. 123–126.

[4] A. J. B. Robertson, *Platinum Metals Review*, 1975, **19**(2), 64–69.

[5] J. Wisniak, *Educación Química*, 2010, **21**(1), 60 – 69.

[6] J. R. Ross in *Heterogeneous Catalysis*, ed. J. R. Ross; Elsevier, Amsterdam, 2012; pp. 1 – 15.

[7] I. Chorkendorff and J. Niemantsverdriet, *Concepts of Modern Catalysis and Kinetics*, WILEY-VCH Verlag GmbH, 2013.

[8] M. Appl, in *Ullmann's Encyclopedia of Industrial Chemistry*, American Cancer Society, 2011; chapter Ammonia, 2. Production Processes.

[9] A. N. Stranges in *Fischer-Tropsch Synthesis, Catalyst and Catalysis*, ed. B. Davis and M. Occelli, Vol. 163 of *Studies in Surface Science and Catalysis;* Elsevier, 2007; pp. 1 – 27.

[10] S. Faramawy, T. Zaki, and A.-E. Sakr, *Journal of Natural Gas Science and Engineering*, 2016, **34**, 34 – 54.

[11] P. Boehm and T. Saba, Identification of natural gas sources using geochemical forensic tools Retrieved 2018-07-23, http://announce.exponent.com/practice/environmental/ef/EF_Notes_Vol_5.pdf, 2009.

[12] Union Gas, Chemical composition of natural gas Retrieved 2018-07-23, https://www.uniongas.com/about-us/about-natural-gas/chemical-composition-of-natural-gas, 2018.

[13] A. Molino, F. Nanna, Y. Ding, B. Bikson, and G. Braccio, *Fuel*, 2013, **103**, 1003 – 1009.

[14] IEA Bioenergy Task 40 and Task 37 Biomethane status and factors affecting market development and trade Technical report, IEA, 2014.

[15] H. Engerer and M. Horn, *Energy Policy*, 2010, **38**(2), 1017 – 1029.

[16] B. Wang, S. Albarracín-Suazo, Y. Pagán-Torres, and E. Nikolla, *Catalysis Today*, 2017.

[17] M. Gambino, R. Cericola, P. Corbo, and S. Iannaccone, *Journal of Engineering for Gas Turbines and Power*, 1993, **115**(4), 747–749.

[18] United Nations Framework Convention on Climate Change, The evolution of catalytic converters https://unfccc.int/process/transparency-and-reporting/greenhouse-gas-data/greenhouse-gas-data-unfccc/global-warming-potentials [accessed in 2019-12-09].

[19] U.S. Environmental Protection Agency, Understanding global warming potentials https://www.epa.gov/ghgemissions/understanding-global-warming-potentials [accessed in 2019-12-09].

[20] E. Makhura, J. Rakereng, O. Rapoo, and G. Danha, *Procedia Manufacturing*, 2019, **35**, 349 – 355.

[21] A. V. Nikitin, A. S. Dmitruk, and V. S. Arutyunov, *Russian Chemical Bulletin*, 2016, **65**(10), 2405–2410.

[22] Y. Hartadi, D. Widmann, and R. J. Behm, *Journal of Catalysis*, 2016, **333**, 238 – 250.

[23] A. Ersson, H. Kušar, R. Carroni, T. Griffin, and S. Järås, *Catalysis Today*, 2003, **83**(1-4), 265–277.

[24] M. Reinke, J. Mantzaras, R. Schaeren, R. Bombach, A. Inauen, and S. Schenker, *Combustion and Flame*, 2004, **136**(1), 217 – 240.

[25] K. Persson, A. Ersson, A. M. Carrera, J. Jayasuriya, R. Fakhrai, T. Fransson, and S. Järås, *Catalysis Today*, 2005, **100**(3-4), 479–483.

[26] P. S. Barbato, A. Di Benedetto, V. Di Sarli, G. Landi, and R. Pirone, *Industrial & Engineering Chemistry Research*, 2012, **51**(22), 7547–7558.

[27] A. D. Benedetto, G. Landi, V. D. Sarli, P. Barbato, R. Pirone, and G. Russo, *Catalysis Today*, 2012, **197**(1), 206 – 213.

[28] A. Di Benedetto, P. S. Barbato, and G. Landi, *Energy & Fuels*, 2013, **27**(10), 6017–6023.

[29] S. Fikri, T. Kasper, U. Bergmann, R. Hegner, and B. Atakan, *Zeitschrift für Physikalische Chemie*, 2015, **229**.

[30] O. Kröcher, M. Elsener, M.-R. Bothien, and W. Dölling, *MTZ worldwide*, 2014, **75**(4), 46–51.

[31] R. Bank, U. Etzien, B. Buchholz, and H. Harndorf, *MTZ Industrial*, 2015, **3**, 14–21.

[32] H. Stotz, L. Maier, and O. Deutschmann, *Topics in Catalysis*, 2017, **60**(1), 83–109.

[33] H. Stotz, L. Maier, A. Boubnov, A. T. Gremminger, J. D. Grunwaldt, and O. Deutschmann, *Journal of Catalysis*, 2019, **370**(October 2019), 152–175.

[34] F. H. Ribeiro, M. Chow, and R. A. Dalla Betta, *Journal of Catalysis*, 1994, **146**(2), 537–544.

[35] M. R. Lyubovsky and L. D. Pfefferle, *Catalysis Today*, 1999, **47**(1-4), 29–44.

[36] W. S. Epling and G. B. Hoflund, *Journal of Catalysis*, 1999, **182**(1), 5 – 12.

[37] P. Thevenin, E. Pocoroba, L. Pettersson, H. Karhu, I. Väyrynen, and S. Järås, *Journal of Catalysis*, 2002, **207**(1), 139 – 149.

[38] I. E. Beck, V. I. Bukhtiyarov, I. Y. Pakharukov, V. I. Zaikovsky, V. V. Kriventsov, and V. N. Parmon, *Journal of Catalysis*, 2009, **268**(1), 60–67.

[39] P. Gélin and M. Primet, *Applied Catalysis B: Environmental*, 2002, **39**(1), 1–37.

[40] P. Gélin, L. Urfels, M. Primet, and E. Tena, *Catalysis Today*, 2003, **83**(1-4), 45–57.

[41] R. Abbasi, L. Wu, S. E. Wanke, and R. E. Hayes, *Chemical Engineering Research and Design*, 2012, **90**(11), 1930–1942.

[42] Z. Li and G. B. Hoflund, *Journal of Natural Gas Chemistry*, 2003, **12**, 153–160.

[43] J. B. Miller and M. Malatpure, *Applied Catalysis A: General*, 2015, **495**, 54–62.

[44] N. M. Kinnunen, J. T. Hirvi, K. Kallinen, T. Maunula, M. Keenan, and M. Suvanto, *Applied Catalysis B: Environmental*, 2017.

[45] M. M. Pakulska, C. M. Grgicak, and J. B. Giorgi, *Applied Catalysis A: General*, 2007, **332**(1), 124–129.

[46] R. J. Farrauto, J. K. Lampert, M. C. Hobson, and E. Waterman M., *Appl. Catal. B: Environ.*, 1995, **6**(95), 263–270.

[47] R. Ramírez-López, I. Elizalde-Martinez, and L. Balderas-Tapia, *Catalysis Today*, 2010, **150**(3-4), 358–362.

[48] L. Ma, S. Yuan, T. Jiang, X. Zhu, C. Lu, and X. Li, *Catalysts*, 2019, **9**(5).

[49] A. York, Global warming potentials (ipcc second assessment report) https://edu.rsc.org/feature/the-evolution-of-catalytic-converters/2020252.article [accessed in 2019-11-05], 2011.

[50] History of the catalytic converter https://www.catalyticconverters.com/history/ [accessed in 2019-11-05].

[51] M. Andersson and J. Froitzheim Technology review - solid oxide cells 2019 Technical Report 2019:601, Energiforsk, 2019.

[52] Fuel Cell Technologies Office, U.S. Department of Energy, Fuel cells https://www.energy.gov/eere/fuelcells/fuel-cells [accessed in 2019-11-05].

[53] G. Towler and R. Sinnott, *Chemical Engineering Design*, Butterworth-Heinemann, Boston, second edition ed., 2012.

[54] M. Schmal, M. M. V. M. Souza, V. V. Alegre, M. A. P. da Silva, D. V. César, and C. A. C. Perez, *Catalysis Today*, 2006, **118**(3), 392–401.

[55] K. Sekizawa, H. Widjaja, S. Maeda, Y. Ozawa, and K. Eguchi, *Catalysis Today*, 2000, **59**(1-2), 69–74.

[56] K. Eguchi and H. Arai, *Applied Catalysis A: General*, 2001, **222**(1-2), 359–367.

[57] R. Kikuchi, S. Maeda, K. Sasaki, S. Wennerström, Y. Ozawa, and K. Eguchi, *Applied Catalysis A: General*, 2003, **239**(1), 169 – 179.

[58] Y. Xin, H. Wang, and C. K. Law, *Combustion and Flame*, 2014, **161**(4), 1048–1054.

[59] S. Fouladvand, S. Schernich, J. Libuda, H. Grönbeck, T. Pingel, E. Olsson, M. Skoglundh, and P. A. Carlsson, *Topics in Catalysis*, 2013, **56**(1-8), 410–415.

[60] P. A. Carlsson, E. Fridell, and M. Skoglundh, *Catalysis Letters*, 2007, **115**(1-2), 1–7.

[61] B. Stasinska, A. Machocki, K. Antoniak, M. Rotko, J. L. Figueiredo, and F. Gonçalves, *Catalysis Today*, 2008, **137**(2), 329 – 334.

[62] R. Kikuchi, S. Maeda, K. Sasaki, S. Wennerström, and K. Eguchi, *Applied Catalysis A: General*, 2002, **232**(1), 23 – 28.

[63] D. Ciuparu, N. Katsikis, and L. Pfefferle, *Applied Catalysis A: General*, 2001, **216**(1), 209 – 215.

[64] S. Colussi, F. Arosio, T. Montanari, G. Busca, G. Groppi, and A. Trovarelli, *Catalysis Today*, 2010, **155**(1), 59 – 65.

[65] P. Velin, M. Ek, M. Skoglundh, A. Schaefer, A. Raj, D. Thompsett, G. Smedler, and P.-A. Carlsson, *The Journal of Physical Chemistry C*, 2019, **123**(42), 25724–25737.

[66] A. W. Petrov, D. Ferri, M. Tarik, O. Kröcher, and J. A. van Bokhoven, *Topics in Catalysis*, 2017, **60**(1), 123–130.

[67] A. W. Petrov, D. Ferri, F. Krumeich, M. Nachtegaal, J. A. van Bokhoven, and O. Kröcher, *Nature Communications*, 2018, **9**(2545).

[68] I. Friberg, N. Sadokhina, and L. Olsson, *Applied Catalysis B: Environmental*, 2019, **250**, 117 – 131.

[69] A. A. Slepterev, V. S. Salnikov, P. G. Tsyrulnikov, A. S. Noskov, V. N. Tomilov, N. A. Chumakova, and A. N. Zagoruiko, *Reaction Kinetics and Catalysis Letters*, 2007, **91**(2), 273–282.

[70] M. Jørgensen and H. Grönbeck, *Topics in Catalysis*, 2019, **62**(7), 660–668.

[71] T. Nilsson Pingel, M. Jørgensen, A. B. Yankovich, H. Grönbeck, and E. Olsson, *Nature Communications*, 2018, **9**(1).

[72] M. Jørgensen and H. Grönbeck, *ACS Catalysis*, 2017, **7**(8), 5054–5061.

[73] M. Jørgensen and H. Grönbeck, *Angewandte Chemie International Edition*, 2018, **57**(18), 5086–5089.

[74] C. Mallika, O. Sreedharan, and J. Gnanamoorthy, *Journal of the Less Common Metals*, 1983, **95**(2), 213 – 220.

[75] J. F. Weaver, C. Hakanoglu, J. M. Hawkins, and A. Asthagiri, *The Journal of Chemical Physics*, 2010, **132**(2), 024709.

[76] A. Hellman, A. Resta, N. M. Martin, J. Gustafson, A. Trinchero, P.-A. Carlsson, O. Balmes, R. Felici, R. van Rijn, J. W. M. Frenken, J. N. Andersen, E. Lundgren, and H. Grönbeck, *The Journal of Physical Chemistry Letters*, 2012, **3**(6), 678–682.

[77] A. Antony, A. Asthagiri, and J. Weaver, *The Journal of chemical physics*, 2013, **139**, 104702.

[78] A. Trinchero, A. Hellman, and H. Grönbeck, *physica status solidi (RRL) - Rapid Research Letters*, 2014, **8**(6), 605–609.

[79] N. M. Martin, M. Van den Bossche, A. Hellman, H. Grönbeck, C. Hakanoglu, J. Gustafson, S. Blomberg, N. Johansson, Z. Liu, S. Axnanda, J. F. Weaver, and E. Lundgren, *ACS Catalysis*, 2014, **4**(10), 3330–3334.

[80] D. Ciuparu, M. R. Lyubovsky, E. Altman, L. D. Pfefferle, and A. Datye, *Catalysis Reviews*, 2002, **44**(4), 593–649.

[81] J. Cortés, E. Valencia, and P. Araya, *Journal of Physical Chemistry C*, 2010, **114**(26), 11441–11447.

[82] M. Van Den Bossche and H. Grönbeck, *Journal of the American Chemical Society*, 2015, **137**(37), 12035–12044.

[83] K. ichiro Fujimoto, F. H. Ribeiro, M. Avalos-Borja, and E. Iglesia, *Journal of Catalysis*, 1998, **179**(2), 431 – 442.

[84] W. R. Schwartz and L. D. Pfefferle, *The Journal of Physical Chemistry C*, 2012, **116**(15), 8571–8578.

[85] J. D. Lee, J. Li, Z. Zhang, and L. Wang, in *Micromechanics and Nanomechanics of Composite Solids*, ed. S. A. Meguid and G. J. Weng, Springer International Publishing, Cham, 2018; chapter 1, pp. 1–38.

[86] W. E and J. Lu, *Scholarpedia*, 2011, **6**(10), 11527.

[87] Q. Y. Luo, Xichun, in *Hybrid Machining - Theory, Methods, and Case Studies*, Elsevier, 2018; chapter 11.1 Introduction.

[88] K. F. Kalz, R. Kraehnert, M. Dvoyashkin, R. Dittmeyer, R. Gläser, U. Krewer, K. Reuter, and J.-D. Grunwaldt, *ChemCatChem*, 2017, **9**(1), 17–29.

[89] *Nature Catalysis*, 2018, **1**(11), 807–808.

[90] K. Reuter, *Oil and Gas Science and Technology*, 2006, **61**(4), 471–477.

[91] H. J. Freund, H. Kuhlenbeck, J. Libuda, G. Rupprechter, M. Bäumer, and H. Hamann, *Topics in Catalysis*, 2001, **15**(2-4), 201–209.

[92] R. Imbihl, R. J. Behm, and R. Schlögl, *Physical Chemistry Chemical Physics*, 2007, **9**(27), 3459.

[93] M. Salciccioli, M. Stamatakis, S. Caratzoulas, and D. G. Vlachos, *Chemical Engineering Science*, 2011, **66**(19), 4319–4355.

[94] M. Maestri, *Chem. Commun.*, 2017, **53**(2011), 10244–10254.

[95] M. K. Sabbe, M.-F. Reyniers, and K. Reuter, *Catalysis Science & Technology*, 2012, **2**(10), 2010–2024.

[96] S. Matera and K. Reuter, *Catalysis Letters*, 2009, **133**(1-2), 156–159.

[97] I. S. Fragkopoulos, I. Bonis, and C. Theodoropoulos, *Multiscale modelling of spillover processes in heterogeneous catalytic systems*, Vol. 30, Elsevier B.V., 2012.

[98] J. Im, H. Shin, H. Jang, H. Kim, and M. Choi, *Nature Communications*, 2014, **5**.

[99] W. Karim, C. Spreafico, A. Kleibert, J. Gobrecht, J. Vandevondele, Y. Ekinci, and J. A. Van Bokhoven, *Nature*, 2017, **541**(7635), 68–71.

[100] M. Mantina, Y. Wang, R. Arróyave, L. Chen, Z. Liu, and C. Wolverton, *Physical review letters*, 2008, **100**, 215901.

[101] J. Hedlund, M. Grahn, D. Korelskiy, M. Rayson, S. Öberg, and P. R. Briddon, *Journal of Membrane Science*, 2012, **415-416**, 271 – 277.

[102] L. M. Molina and B. Hammer, *Phys. Rev. Lett.*, 2003, **90**, 206102.

[103] G. N. Vayssilov, Y. Lykhach, A. Migani, T. Staudt, G. P. Petrova, N. Tsud, T. Skála, A. Bruix, F. Illas, K. C. Prince, V. Matolín, K. M. Neyman, and J. Libuda, *Nature Materials*, 2011, **10**(4), 310–315.

[104] P. A. M. Dirac, *Proceedings of the Royal Society of London. Series A, Containing Papers of a Mathematical and Physical Character*, 1929, **123**(792), 714–733.

[105] L. Grajciar, C. J. Heard, A. A. Bondarenko, M. V. Polynski, J. Meeprasert, E. A. Pidko, and P. Nachtigall, *Chem. Soc. Rev.*, 2018, **47**, 8307–8348.

[106] S. Karabasov, D. Nerukh, A. Hoekstra, B. Chopard, and P. V. Coveney, *Philosophical Transactions of the Royal Society A: Mathematical, Physical and Engineering Sciences*, 2014, **372**(2021), 20130390.

[107] P. V. Coveney, J. P. Boon, and S. Succi, *Philosophical Transactions of the Royal Society A: Mathematical, Physical and Engineering Sciences*, 2016, **374**(2080), 20160335.

[108] A. G. Hoekstra, S. Portegies Zwart, and P. V. Coveney, *Philosophical Transactions of the Royal Society A: Mathematical, Physical and Engineering Sciences*, 2019, **377**(2142), 20180355.

[109] K. Delgado, L. Maier, S. Tischer, A. Zellner, H. Stotz, and O. Deutschmann, *Catalysts*, 2015, **5**(2), 871–904.

[110] S. Kannepalli, A. Gremminger, S. Tischer, and O. Deutschmann, *Chemical Engineering Science*, 2017, **174**, 189–202.

[111] N. Argaman and G. Makov, *American Journal of Physics*, 2000, **68**(1), 69–79.

[112] Y. B. Band and Y. Avishai in *Quantum Mechanics with Applications to Nanotechnology and Information Science*, ed. Y. B. Band and Y. Avishai; Academic Press, Amsterdam, 2013; pp. 871 – 889.

[113] H. Eyring, *The Journal of Chemical Physics*, 1935, **3**(2), 107–115.

[114] M. G. Evans and M. Polanyi, *Trans. Faraday Soc.*, 1935, **31**, 875–894.

[115] A. Jansen, *An Introduction to Kinetic Monte Carlo Simulations of Surface Reactions*, Springer, Berlin, Heidelberg, 2012.

[116] V. P. Zhdanov, *Elementary Physicochemical Processes on Solid Surfaces*, Springer, Boston, MA, 1991.

[117] J. B. Anderson, *Chemical Engineering Science*, 1963, **18**, 147–148.

[118] T. Shamim, *International Journal of Engine Research*, 2003, **4**(2), 129–141.

[119] F. B. Salisbury, P. F. Wareing, G. H. Yeoh, C. Liu, , and J. Tu, in *Computational Fluid Dynamics, Second Edition*, London: Elsevier Science & Technology, 2012; chapter 7 Some Applications of CFD with Examples, pp. 275–348.

[120] T. Enrico and F. Pio, *AIChE Journal*, 1992, **38**(2), 201–210.

[121] R. Hawthorne, *AIChE Symp. Ser.*, 1974, **70**, 428.

[122] K. C. Metaxas and N. G. Papayannakos, *Chemical Engineering Journal*, 2008, **140**(1), 352 – 357.

[123] A. Şahin, E. Alp, D. Eserci, and H. C. Cabbar, *Chemical Engineering Communications*, 2017, **204**(10), 1129–1142.

[124] K. P. de Jong, in *Catalysis From Principles to Applications*, ed. M. Beller, A. Renken, and R. A. van Santen, WILEY-VCH Verlag GmbH, 2012; chapter 20 Preparation of Supported Catalysts, pp. 420–429.

[125] I. Chorkendorff and J. Niemantsverdriet, in *Concepts of Modern Catalysis and Kinetics*, WILEY-VCH Verlag GmbH, 2013; chapter 5.5 Preparation of Supported Catalysts, pp. 203–206.

[126] S. Brunauer, P. H. Emmett, and E. Teller, *Journal of the American Chemical Society*, 1938, **60**(2), 309–319.

[127] I. Chorkendorff and J. Niemantsverdriet, in *Concepts of Modern Catalysis and Kinetics*, WILEY-VCH Verlag GmbH, 2013; chapter 5.3 Characteristics of Small Particles and Porous Material, pp. 187–196.

[128] E. P. Barrett, L. G. Joyner, and P. P. Halenda, *Journal of the American Chemical Society*, 1951, **73**(1), 373–380.

[129] H. Günzler and H.-U. Gremlich, *IR Spectroscopy An Introduction*, WILEY-VCH Verlag GmbH, 2002.

[130] A. Trinchero, A. Hellman, and H. Grönbeck, *Surface Science*, 2013, **616**.

[131] R. Burch, F. Urbano, and P. Loader, *Applied Catalysis A: General*, 1995, **123**(1), 173–184.

[132] R. Monteiro, D. Zemlyanov, J. Storey, and F. Ribeiro, *Journal of Catalysis*, 2001, **199**(2), 291 – 301.

[133] G. Zhu, J. Han, D. Y. Zemlyanov, and F. H. Ribeiro, *The Journal of Physical Chemistry B*, 2005, **109**(6), 2331–2337.

[134] R. E. Hayes, S. T. Kolaczkowski, P. K. Li, and S. Awdry, *Chemical Engineering Science*, 2001.

[135] A. Hinz, M. Skoglundh, E. Fridell, and A. Andersson, *Journal of Catalysis*, 2001, **201**(2), 247 – 257.

[136] S. Chilukoti, F. Gao, B. G. Anderson, J. W. H. Niemantsverdriet, and M. Garland, *Phys. Chem. Chem. Phys.*, 2008, **10**, 5510–5520.

[137] D. L. Mowery, M. S. Graboski, T. R. Ohno, and R. L. McCormick, *Applied Catalysis B: Environmental*, 1999, **21**(3), 157 – 169.

[138] D. L. Mowery and R. L. McCormick, *Applied Catalysis B: Environmental*, 2001, **34**(4), 287 – 297.

[139] M. Monai, T. Montini, C. Chen, E. Fonda, R. J. Gorte, and P. Fornasiero, *ChemCatChem*, 2015, **7**(14), 2038–2046.

Appendix

Reactor model

For a clearer view of the computational approach the discretized equations describing the flow-reactor model are outlined here. The reactor is discretised into 10 tanks-in-series (k) while the porous catalyst is divided into 12 sublayers (n) to account for internal mass and heat transport axially and radially. The length of the tanks and the thickness of the layers increase successively with 30 % from the inlet and 50 % from the catalyst surface, respectively.

The mass balance for the bulk gas phase (n=0) in each tank is described as

$$0 = (F_{i,k-1} - F_{i,k}) - \Gamma_{i,k,0} \cdot (C_{i,k,0} - C_{i,k,1})$$

where F is the molar flow and C is the gas concentration for gas component *i* in tank *k*. Γ is the lumped mass transport coefficient and further described below.

The internal gas composition, in each sublayer (n≥1), is described by a mass balance equation where the effective diffusivity and reaction are included. The mass balance for component *i* in sublayer *k* (*k*=0 for the bulk gas phase) is described as

$$0 = \Gamma_{i,k,n-1} \cdot (C_{i,k,n-1} - C_{i,k,n}) - \Gamma_{i,k,n} \cdot (C_{i,k,n} - C_{i,k,n+1}) + \sum_{n} \nu_i \cdot r_{k,n} \cdot c_{site} \cdot m_{k,n}$$

where ν is the stoichiometric coefficient, *r* is the reaction rate, c_{site} is the density of active sites, *m* is the mass of catalyst in tank *k* and sublayer *n*. No mass transport occurs between the innermost sublayer and the corderite monolith substrate, hence, the second term in the equation above is ignored when n=12 (the innermost sublayer).

The heat balance for the bulk gas phase in each tank is described as

$$0 = \frac{1}{C_{P,k} \cdot V_k \cdot C_{tot,k}} \cdot (F_k \cdot C_p \cdot T_{g,k} - h_{k,k} \cdot A_k \cdot (T_{g,k} - T_{s,k}))$$

where C_p is the heat capacity, V is the tank volume, C_{tot} is the total gas concentration, h_k is the heat transport coefficient, A is the area available for heat transport, T_g is the gas phase temperature and T_s is the catalyst surface temperature for tank *k*.

According to the Anderson's criterion [117], the catalyst layer can be assumed to be

isothermal in radial direction. The temperature of the porous catalyst is described as

$$0 = \frac{1}{C_{Pcat} \cdot m_{cat,k}} \cdot (h_{k,k} \cdot A_k \cdot (T_{g,k} - T_{s,k}) - A_s \cdot (Q_{k+1} - Q_k) + \sum_n m_{cat,k,n} \cdot r_{k,n} \cdot c_{site} \cdot (-\Delta H_r))$$

where C_{Pcat} is the heat capacity of the porous catalyst, $h_{k,k}$ is the heat transfer coefficient in tank k, A_s is the cross sectional area of the porous catalyst and ΔH_r is the reaction enthalpy. Q is the solid heat flux is described as

$$Q_k = -2 \cdot \lambda \cdot (T_{s,k} - T_{s,k-1})/(\Delta x_k + \Delta x_{k-1}) \qquad for\ k \neq 1, 10$$

$$Q_k = -\epsilon \cdot \sigma \cdot (T_{s,k}^4 - T_{in,k}^4) \qquad for\ k = 1$$

$$Q_k = -\epsilon \cdot \sigma \cdot (T_{s,k}^4 - T_{g,k}^4) \qquad for\ k = 10$$

where λ is the heat conductivity of the porous catalyst, Δx_k is the length of tank k, ϵ is the emissivity factor (set to 0.6), σ is the Stefan–Boltzmann constant and T_{in} is the feed gas temperature.

The lumped mass transport coefficient, $\Gamma_{i,k}$, is expressed through the general mass transport equation where equimolar counter diffusion is assumed to prevail. The general mass transport equation for molar flux (N) is then expressed as

$$N_{i,k,n} = -D_{eff,i,k} \cdot \frac{dC_i}{dx}$$

The molar flux between the catalyst surface and the first layer can then be expressed as

$$N_{i,k,n} = -D_{eff,i,k} \cdot \frac{C_{i,k,1} - C_{i,k,surface}}{0.5 \cdot \Delta z_1}$$

where Δz_1 is the thickness of the first sublayer of the porous catalyst.

By setting the above expression equal to the mass transport from the bulk gas phase to the catalyst surface as

$$N_{i,k,n} = -D_{eff,i,k} \cdot \frac{C_{i,k,1} - C_{i,k,surface}}{0.5 \cdot \Delta z_1} = k_{c,i,k} \cdot (C_{i,k,0} - C_{i,k,surface})$$

where k_c is the mass transport coefficient as described in section 3.1.3. By rearranging the above expression the lumped mass transport coefficient, Γ is obtained as

$$N_{i,k,0} \cdot A_k = \frac{A_k}{\frac{1}{k_{c,i,k}} + \frac{0.5 \cdot \Delta z_1}{D_{eff,i,k}}} \cdot (C_{i,k,0} - C_{i,k,1}) = \Gamma_{i,k,0} \cdot (C_{i,k,0} - C_{i,k,1})$$

Similarly for subsequent sublayers (n≥1)

$$N_{i,k,n} \cdot A_k = \frac{A_k}{\frac{0.5 \cdot \Delta z_n}{D_{eff,i,k}} + \frac{0.5 \cdot \Delta z_{n+1}}{D_{eff,i,k}}} \cdot (C_{i,k,n} - C_{i,k,n+1}) = \Gamma_{i,k,n} \cdot (C_{i,k,n} - C_{i,k,n+1})$$

where $k_{c,i,k}$ is calculated as outlined in section 3.1.3.